Determination of mass loadings and plume heights of volcanic ash clouds from satellite data

A. J. Prata and I. F. Grant

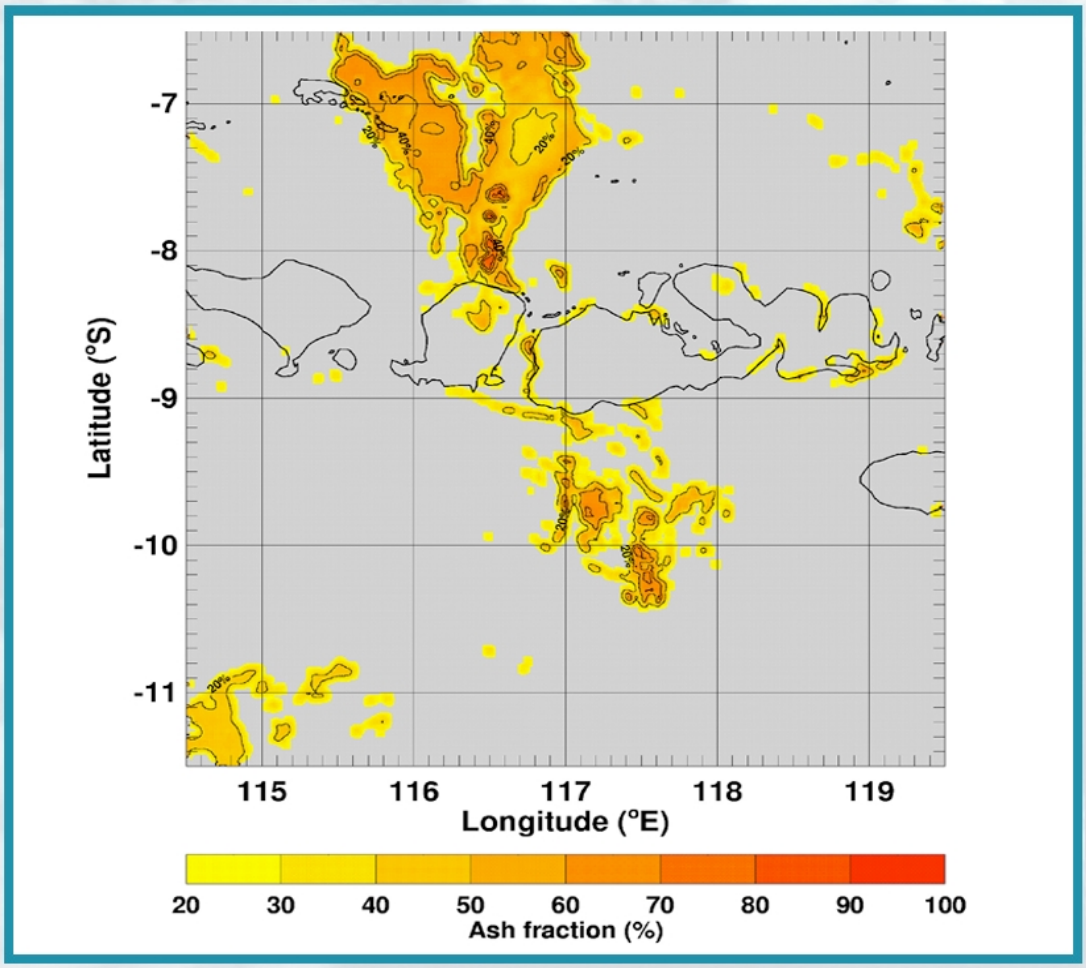

CSIRO

Atmospheric Research

CSIRO Atmospheric Research Technical Paper No. 48

National Library of Australia Cataloguing-in-Publication Entry

Prata, A. J. (Alfredo J.)
Determination of mass loadings and plume heights of volcanic ash clouds from satellite data.

Bibliography.
ISBN 0 643 06639 X.

1. Remote sensing. 2. Volcanoes - Volcanic ash clouds - Satellites. I. CSIRO. Division of Atmospheric Research. II. Title. (Series : CSIRO Atmospheric Research technical paper ; no. 48).

621.3678

Address and contact details:
CSIRO Atmospheric Research
PB 1, Aspendale, Victoria 3195, Australia
Ph: (+61) 3 9239 4681; Fax: (+61) 3 9239 4444
http://www.dar.csiro.au
Email: Chief@dar.csiro.au

CSIRO Atmospheric Research Technical Papers may be issued out of sequence. From July 2000, all new Technical Papers will appear on the Web site of CSIRO Atmospheric Research. Some Technical Papers will also appear in paper form.

Determination of mass loadings and plume heights of volcanic ash clouds from satellite data.

A. J. Prata and I. F. Grant
CSIRO Atmospheric Research
Private Bag 1, Aspendale
Vic 3195, Australia

Abstract

A retrieval scheme for determining some microphysical properties of volcanic ash clouds from thermal infrared satellite data is described. The mathematical details are provided here, while the broader implications of this research are outlined in a paper published by the *Quarterly Journal* (Prata and Grant, 2001). The report also provides details of the methods used to determine ash cloud heights from their shadows cast on land or ocean. The optical properties of a model andesite ash cloud are tabulated. These may be used in conjunction with data from advanced satellite sensors to infer ash cloud microphysics.

Radiative transfer (RT) calculations were also performed to investigate the relationship between top-of-the-atmosphere brightness temperatures (or radiances) in the split-window channels and water vapour amount for some current and planned satellite radiometers (e.g. AVHRR, ATSR-2, GMS-5 and GLI). The input data to the RT model come from the NCEP re-analysis and provide information on a spatial scale of 2.5 x 2.5 degrees and temporal resolution of 6 hours.

Strong correlations were found between the difference in brightness temperatures (referred to as T_4-T_5) in the split-window channels and precipitable water, and between brightness temperature in one channel and precipitable water. Thus it follows that the relationship between the brightness temperature in one channel and the brightness temperature difference is a strong function of the precipitable water. Based on this, an empirical relationship is developed to describe the behaviour of T_4-T_5 as a function of T_4 for global conditions. The relationship is then used to provide a water vapour correction for a modified volcanic ash detection scheme. The modified scheme retrieves the fraction of ash present in a pixel and is based on a simple model of the T_4-T_5 signature arising from ash and the empirical water vapour correction formula. Image-based estimates of the clear-sky, ash-free T_4-T_5, the cloud-top temperature and the clear-sky surface temperature are required. Results using the modified scheme are shown for four test case eruptions.

1 Introduction

This report provides some mathematical details for determining mass loadings, plume heights and other cloud microphysical properties of volcanic ash clouds using satellite data. The report should be read in conjunction with a paper by the same authors published in the *Quarterly Journal of the Royal Meteorological Society* which provides the broader basis for this research, its context and usefulness to the aviation community. Apart from the more detailed mathematical descriptions provided here, some of the illustrations have been produced in colour, which aids in their interpretation, and there is an additional Table and some new results on a water vapour correction method.

The basic purpose of this research is to provide robust retrieval procedures for interpreting and quantitatively deriving microphysical properties of ash clouds. By understanding these properties it is hoped that operational procedures for the avoidance of hazardous volcanic ash clouds by aviation can be improved.

The report begins with a description of the radiative transfer procedures used to develop a retrieval scheme for deriving the particle sizes and mass loadings in volcanic ash clouds by utilising infrared radiation. The calculations are extended to cover the range of wavelengths likely to be available from existing or proposed satellite instruments. A tabulation of the optical parameters for this model is provided in this report.[1] The model is used to derive mass loadings for some eruptions from Mt. Ruapehu in New Zealand. Cloud height retrieval procedures are described next and a section is devoted to the mathematical details for the determination of cloud height from its shadow. The third part of the report includes a description of a new method for correcting infrared window radiances for the effects of water vapour. An illustration is given on how the method might work in practice using eruptions from Rindjani volcano in Indonesia.

2 Retrieval method

The radiative transfer required to extract quantitative information from infrared window radiances (8–12 μm) employs Mie theory and plane parallel radiative transfer in an absorbing and scattering cloud. Given the real and imaginary parts of the index of refraction of the ash-cloud particle as a function of wavelength, and the particle shape and size distribution, the efficiencies for scattering, absorption and extinction are calculated using a Mie scattering program. There is scant information on particle shapes in real ash clouds and only approximate methods exist for calculating efficiencies for particles of arbitrary shapes. We assume that the particles are spherical and the exact Mie-theory computer program of Evans (1988) is employed to calculate the efficiencies. Some measurements exist for the particle size distribution at the edges of the Mt. St. Helens ash cloud (see the papers in Newell and Deepak, 1982). These data indicate that a log-normal (or Zold) size distribution gives a reasonable fit to the distribution. The

[1] A graphical presentation was given in the paper by Prata and Grant (2001).

measurements reported by King *et al.,* (1984) and Hoffman and Rosen (1984) of the El Chichón stratospheric aerosol layer fit a modified-γ size distribution quite well. These data generally pertain to volcanic aerosol layers that are relatively old and high in the atmosphere. For this work, where only the fine particles can be detected in the nascent and low (tropospheric) volcanic plumes, we assume that the size distributions would be similar. We used both size distributions to perform the radiative transfer calculations, and although there were differences in detail between the results for the two distributions, the basic results and mass loadings were essentially the same.

The parameters used in the Mie program are described in Prata (1989b). Once the Mie program has been run for each value of the size parameter (mean particle size and monochromatic wavelength), scattering parameters are then fed into a plane-parallel discrete ordinates radiative transfer program (Stamnes and Swanson, 1981). Given the single scattering albedo, asymmetry parameter, extinction and scattering efficiencies as a function of monochromatic wavelength, and the cloud-top and surface temperatures, radiances emerging from the top of the cloud along n distinct streams (zenith angles) are computed. These radiances are calculated for cloud optical depths ranging from 0 to 20 at wavelengths corresponding to AVHRR-2 channels 4 and 5, and ATSR-2 11 μm and 12 μm channels. At the completion of these calculations, a large two-dimensional look-up table exists with entries at prescribed values of the mean particle size r_m and optical depth τ. Each entry in the table consists of pairs of brightness temperatures T_4 and T_5. The retrieval then consists of locating the (r_m, τ) pairs within the look-up table that best match (T_4, T_5) pairs of AVHRR-2 or ATSR-2 measurements at each image pixel.

The calculations were performed assuming that there is no absorption of infrared radiation by water vapour. This is not correct, but the effect of water vapour absorption on the results is small for the volcanic plumes studied here. The effects of atmospheric water vapour absorption on the satellite brightness temperatures have been assessed by performing radiative transfer calculations. The radiative transfer model Modtran 3 (Berk *et al.*, 1989), was used to calculate the temperature difference between the the satellite measured brightness temperatures at 11 μm and 12 μm wavelengths, at each vertical level using the temperature and moisture structure from a nearby radiosonde profile. The results of this analysis are shown in Figure 3. The effect of water vapour is greatest at the lowest levels, where it exceeds 1 K. At higher levels, near to the location of the plume, the effect is less than 0.2 K. In the tropics and in high humidity conditions, the effect of water vapour absorption can mask out the 'reverse' absorption effect of volcanic ash clouds. This can lead to misidentification of volcanic clouds and is a limitation of the current thermal detection method.

Size distributions, scattering parameters and mass loading

The modified-γ distribution has the functional form,

$$n(r) = N_o \frac{r^\alpha}{\Gamma[\frac{\alpha+1}{\gamma}]} b^{\frac{\alpha+1}{\gamma}} \exp(-br^\gamma), \tag{1}$$

where $n(r)$ is the number of particles per unit volume, r is the particle radius, Γ is the Gamma function (see Press *et al.*, 1986, page 156), N_o, b, α, and γ are parameters of the distribution. The size parameter, x, is related to the particle radius and the wavelength λ through,

$$x = \frac{2\pi r}{\lambda}. \tag{2}$$

Used here, γ=1, α=6, $b = 6/r_o$, and (6) reduces to,

$$n(x) = Cx^6 \exp\left(-\frac{6x}{x_o}\right),$$

where C is a constant replacing the other parameters. Within a distribution of sizes, the mode radius r_o corresponds to a mode size parameter x_o.

The log-normal distribution is described by,

$$n(x) = N_o \frac{1}{\sigma_x} \exp\left[-\frac{(Ln(x) - Ln(x_o))^2}{2\sigma_x^2}\right], \tag{3}$$

where, as before x is the size parameter. The parameter $\sigma_x = 2\pi\sigma_r/\lambda$ is related to the standard deviation (σ_r) of the distribution and is a measure of its spread. In the calculations performed with this distribution, σ_r was set to 0.5, 0.75, 1.0 and 1.25 μm, and results are reported for σ_r=1.0 μm.

The inputs to the Mie program are the real and imaginary parts of the refractive index (m), the size parameter and the size distribution. The outputs are the extinction efficiency ($\hat{Q}_{ext}$) and scattering efficiency ($\hat{Q}_{sca}$) and phase function ($P(\theta)$). For polydispersions these efficiency factors are related to the single particle efficiencies (Q_f)by,

$$\hat{Q}_f = \frac{\int_o^\infty \pi r^2 Q_f(\frac{2\pi r}{\lambda}, m)\frac{dn(r)}{dr}dr}{\int_o^\infty \pi r^2 \frac{dn(r)}{dr}dr}. \tag{4}$$

The absorption efficiency is,

$$\hat{Q}_{abs} = \hat{Q}_{ext} - \hat{Q}_{sca}. \tag{5}$$

The remaining parameters that are needed to perform the radiative transfer calculations and which relate to the cloud microphysical structure are: The single scattering albedo,

$$\varpi = \frac{\hat{Q}_{ext}}{\hat{Q}_{sca}}, \tag{6}$$

the asymmetry parameter,

$$g = \frac{1}{2}\int_{-1}^{1} P(\theta)\cos\theta d\cos\theta, \tag{7}$$

where θ is the scattering angle. The number of particles per unit volume in the cloud is,

$$N = \int_o^\infty \frac{dn}{dr}dr, \tag{8}$$

and the optical depth of the cloud is,

$$\tau_\lambda = \pi L \int_o^\infty r^2 Q_{ext}(r,\lambda) n(r) dr, \tag{9}$$

where L is the geometrical thickness of the cloud. The mass loading (kg m^{-3}) is

$$M = \frac{4\pi}{3}\rho \int_o^\infty r^3 n(r) dr, \tag{10}$$

where ρ is the density of the ash. The total mass can be calculated by multiplying (15) by the volume of a pixel (geometric thickness multiplied by the area of a pixel).

Retrieval procedure

In the (T_4, $T_4 - T_5$) plane there exist isolines of constant mean particle radius, r_m^j. Each point on the isoline, r_m^j corresponds to particular values of the optical depth, $\tau^{j,i}$. Lines connecting equal values of $\tau^{j,i}$ also exist. Given the measured values (T_4^*, T_5^*), the retrieval procedure requires us to find the 'best' values of (τ, r_m). A linear interpolation procedure is adopted:

- Find values of $T_4(\tau^{j,i}, r_m^j)$ that bracket T_4^*. Label these $T_4^1(r_m^j)$, $T_4^2(r_m^j)$,$T_4^1(r_m^{j+1})$,$T_4^2(r_m^{j+1})$
- Interpolate on the r_m^j isolines to find the appropriate $\Delta T(r_m^j)$ (= $T_4(r_m^j) - T_5(r_m^j)$).

$$\Delta T(r_m^j) = w_1 \Delta T_2(r_m^j) + (1 - w_1)\Delta T_1(r_m^j),$$

$$w_1 = \frac{T_4^1(r_m^j) - T_4^*}{T_4^1(r_m^j) - T_4^2(r_m^j)}.$$

  Similarly for $\Delta T(r_m^{j+1})$:

$$\Delta T(r_m^{j+1}) = w_2 \Delta T_2(r_m^{j+1}) + (1 - w_2)\Delta T_1(r_m^{j+1}),$$

  and the weight w_2 is defined in an analogous way to w_1.

- The required mean particle radius is obtained using linear interpolation,

$$r_m^* = w_r r_m^j + (1 - w_r) r_m^{j+1},$$

$$w_r = \frac{\Delta T(r_m^{j+1}) - \Delta T^*}{\Delta T(r_m^{j+1}) - \Delta T(r_m^j)}.$$

- In practice there are n isolines of $r_m^j, j = 1, n$ and n is small ($n = 18$), and many more values of $\tau^{j,i}, i = 1, k$ ($k = 100$ is used in the current software). Thus $2nxk$ values of ΔT are precomputed.

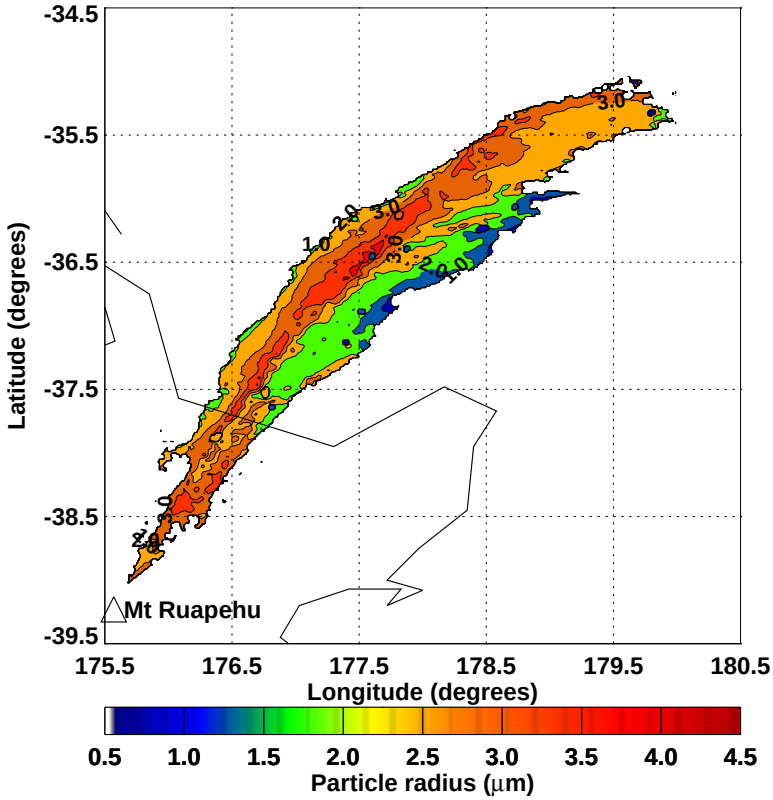

Figure 4. Particle size retrieval for the eruption of 17 June 1996 using AVHRR-2 data.

3 Particle radius retrievals

Figure 4 shows a contour plot of mean particle radius retrieved from the AVHRR-2 image shown in Figure 1(a). The largest particles (up to ≈ 4 μm radii) are found around the middle of the plume and in 'clumps' distributed non-uniformly along the plume. Some large particles found at the edges may be an artifact of the analysis because these regions are quite transparent and as explained previously it is possible that the entrainment of ambient (water-rich) air may be significant. There are, however, closed contours within the plume with congregations of large particles. There appears to be an elongation of the particle size contours in the direction of the wind at that level. There also appears to be a gradient in particle size from smallest particles in the southeastern side of the plume, to largest particles in the northwestern side of the plume.

Figure 5 shows the frequency distribution of particle sizes in the plumes for both size distribution models. Particle sizes vary from 1 μm up to ≈ 4 μm, with mode maxima near 3 μm. There is some evidence of multiple modes within the distribution and such behaviour has been found for the Fuego and Santiago ash clouds (Cadle *et al.*, 1979), the Mt. St. Helens ash cloud (Chuan *et al.*, 1981; Farlow *et al.*, 1981), and the Agung ash clouds (Mossop, 1964). Chuan *et al.* (1981) found a mode peak at radius ≈ 2.5 μm from monitoring continuous emissions from Mt. St. Helens, prior to a strong eruption on August 7 1980.

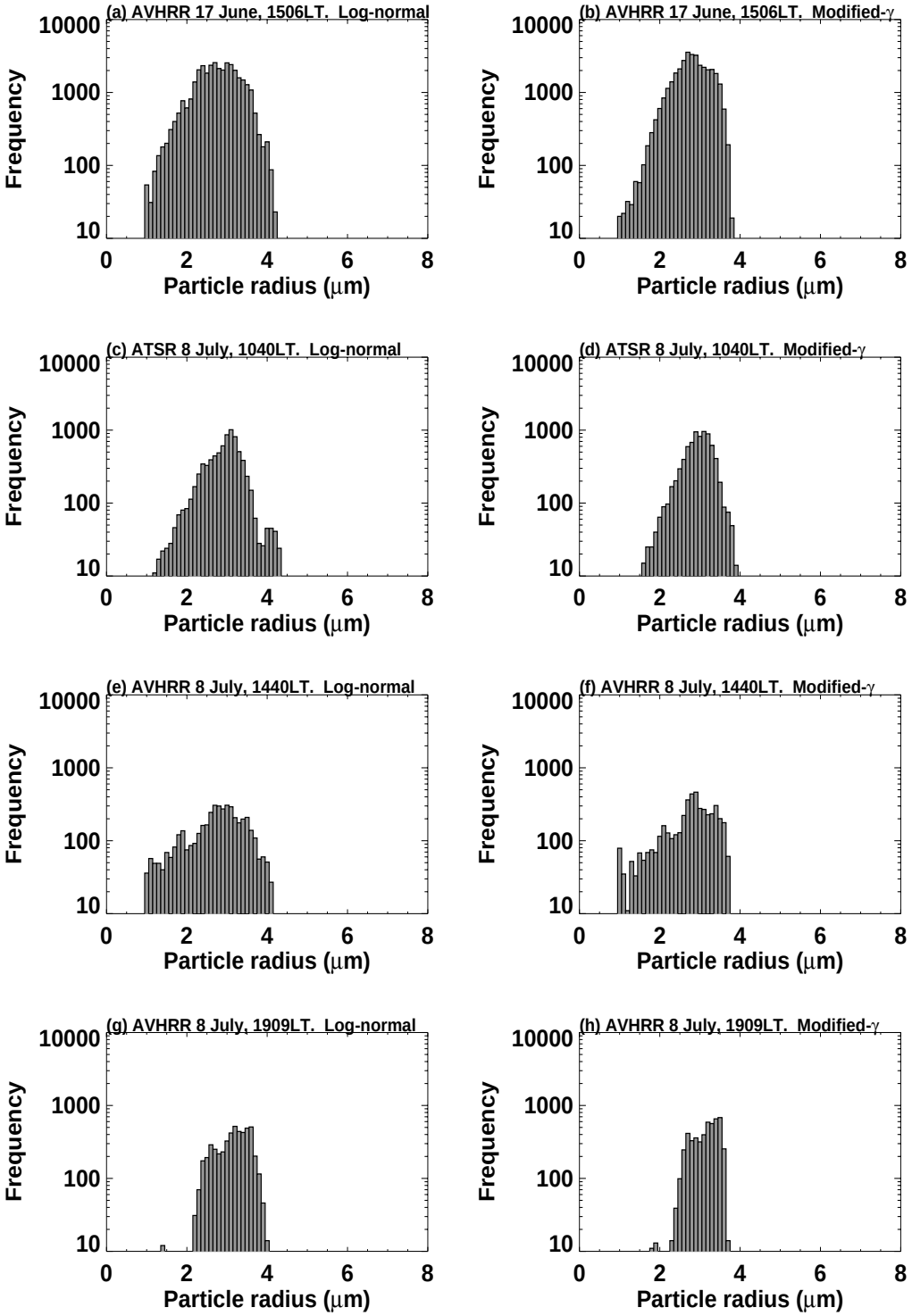

Figure 5. Retrieved particle size histograms for four Ruapehu plumes and two model size distributions.

4 Mass loadings

The U. S. Military consider mass loadings $>$ 50 mg m^{-3} a potential hazard to their aircraft operations. Przedpelski and Casadevall (1994) estimated a mass loading of $\approx$ 2000 mg m^{-3} at 25,000 ft ($\approx$ 7.5 km) for the 15 December 1989 Redoubt eruption cloud that caused significant damage to a KLM Boeing 747-400 jet aircraft. Mass loadings include all particles with radii < 50 μm, which have atmospheric residence times of the order of at least a few hours. Having determined the particle size distribution, the geometrical thickness of the cloud and its areal extent, it is possible to estimate the mass loading of fine particles in each of the plumes studied here. The density of the ash is taken to be 2600 kg m^{-3} and the area of a pixel is taken as 1.2 x 1.2 km^2 – this is a mean area for pixels for both the AVHRR-2 and ATSR-2. Pixels are counted if they satisfy criterion (1), and the retrieved particle size is in the range $1 < r_m < 8$ μm. An estimate of the cloud thickness is crucial to the evaluation of mass loadings. Data on cloud thicknesses are not available so they must be estimated by other means. Studies of plume rise in stable stratified atmospheres (e.g. Briggs, 1975) suggest that to a reasonable approximation the vertical extent of a plume can be estimated from the cloud-top height. For example, Manins (1985) has calculated the heights and vertical extents of stabilized smoke plumes as a function of power release and following Briggs (1975) suggests that the vertical extent (cloud thickness), Δz, of these plumes is given by,

$$\Delta z = 0.4 z_{top},$$

where z_{top} is the height of the plume top. The cloud-top heights calculated previously for the Ruapehu plumes suggest a cloud thickness range of 1.5–3.0 km, with a likely error of $\pm$0.5 km. The variability of cloud thickness along the plumes and the problem of not having simultaneous plume-top height and plume-base height data for each of the plumes, means that we cannot estimate plume thickness to any greater accuracy. The mass loading (kg m^{-3}) is

$$M = \frac{4\pi}{3}\rho \int_o^\infty r^3 n(r) dr, \tag{11}$$

where ρ is the density of the ash and $n(r)$ is the size distribution. The total mass can be calculated by multiplying (6) by the volume of a pixel (geometric thickness multiplied by the area of a pixel). Table 1 lists the results obtained for all four plumes using both size distributions.

Table 1: Retrieved mass loadings and mode radii for the two size distributions used and for four Ruapehu plumes. The range of mass loadings shown corresponds to a range in cloud thickness from 1.5 km to 3.0 km.

Date:Time	Sensor	Size distribution			
		Log-normal		Modified–γ	
		Mass loading (mg m^{-3})	Mode radius (μm)	Mass loading (mg m^{-3})	Mode radius (μm)
17-06-96:1506	AVHRR-2	3.5–6.9	2.7	3.2–6.3	2.7
08-07-96:1040	ATSR-2	1.4–2.7	3.1	1.4–2.6	3.1
08-07-96:1440	AVHRR-2	1.5–2.9	3.0	1.4–2.6	2.9
08-07-96:1909	AVHRR-2	1.7–3.2	3.2	1.5–2.9	3.5

The retrievals for the 8 July plumes should be comparable, as the time difference between the AVHRR-2 and ATSR-2 data acquisitions is not long (less than five hours) and the eruptions during these days were similar in nature. The mode radii on all days are similar, but the mass loading differences between the June eruption and the July events are probably significant.

Hobbs *et al.* (1981) made aircraft-based measurements of the size distributions and number densities of ash in the periphery of the Mt. St. Helens plume. Some measurements were made at 3 km altitude and 9.3 km downwind of the volcano and these can be compared with our results. For particles in the size range 1–5 μm, the number density is of the order 10–1 cm^{-3} (see Fig. 2B of Hobbs *et al.*, 1981), which correspond to mass loadings of 0.1–1.0 mg m^{-3}. Sehmel (1982) also reported mass loadings in the range 1–10 mg m^{-3} in the dispersed Mt. St. Helens volcanic cloud. Our results may also be compared with silicate mass loading retrievals by Yu and Rose (1999) for the El Chichón clouds, and from recent estimates made by W. I. Rose for the June - September 1992 Spurr eruptions (personal communication). These mass loadings were found to be in the range 1–5 mg m^{-3}. Wen and Rose (1994) determined the total mass of fine particles for the August 19 1992 Crater Peak/Spurr eruption and obtained a value of 0.2 x 10^6 t. They estimated the cloud area to be 10^5 km^2, giving a mass loading range of 1.5–3.0 mg m^{-3} for a cloud thickness range of 1.5–3.0 km. Wen and Rose also show that their total mass estimates are not significantly affected by the choice of size distribution.

The mean retrieved mass loadings are an order of magnitude smaller than the value considered hazardous to aircraft (cf. $\approx$ 50 mg m^{-3} or greater). The mass loadings calculated here represent only those particles in the restricted size range, $1 < r < 8$ μm, and these represent only a small fraction of the total mass of ejected matter. However, these are the particles which are most hazardous to jet engines and it would appear to be necessary to develop a mass loading threshold based on particles in this size range. The mass in this size range typically represents $\approx$ 1% of the total mass ejected (e.g. Wen and Rose, 1994; Bursik *et al.*, 1994), which suggests a *total* mass loading of 100–500 mg m^{-3} for the Ruapehu clouds and thus they would have been a threat to jet aircraft.

5 Volcanic cloud model

The new (e.g. MODIS) and proposed advanced multispectral sensors (e.g. GLI, SEVIRI) include many channels capable of providing detection and discrimination of volcanic ash clouds. A model of an ash cloud has been developed in order to exploit these new sensors. We include information from the visible to infrared–although most of the discussion has centred on the infrared window radiances, it seems likely that the visible and near infrared data may also provide a means for ash cloud detection.

At near infrared wavelengths (e.g. λ=1.61 μm) ice clouds appear much darker than clouds of water droplets, because the imaginary part of the refractive index of ice is larger than that of water at this wavelength and consequently ice absorbs more strongly at this wavelength. A comparison of the refractive indices of water, ice and andesite (a common constituent of ash clouds) is given in Table 2.

Table 2: Refractive indices for water, ice and andesite (a silica-rich mineral). The last column gives the reference to the origin of the data shown.

Wavelength (μm)	n_r	n_i	Reference
Ice			
0.63	1.309	1.04E-8	Masuda and Takashima (1990)
1.61	1.289	3.41E-4	Masuda and Takashima (1990)
Water			
0.63	1.332	1.44E-8	Masuda and Takashima (1990)
1.61	1.317	0.87E-4	Masuda and Takashima (1990)
Andesite			
0.68	1.470	1.70E-3	Pollack *et al.* (1973)
1.61	1.470	3.30E-3	Pollack *et al.* (1973)

Pollack *et al.* (1973) list refractive indices of andesite (and some other minerals) over a large range of wavelengths from the UV to the infrared. These data are not the only source of refractive index values for minerals; see for example, Volz (1973), Ivlev and Popova (1973) and Sokolik and Toon (1999). We have used the Pollack *et al.* values as a starting point to provide the input optical parameters required for more detailed radiative transfer calculations, and we propose a model of a volcanic ash cloud based on the Pollack *et al.* refractive indices of andesite. The ash cloud model consists of spherical andesite particles in a log-normal size distribution with a mean particle radius of 3 μm. The single-scatter albedo, asymmetry parameter and coefficients of absorption, scattering and extinction are calculated for the polydisperse particle size distribution using the Mie program discussed earlier. Table 3 provides a listing of the the variation of single-scatter albedo (ϖ), extinction coefficient (Q_{ext}), and asymmetry parameter (g) for wavelengths ranging from 0.3 μm to 14.5 μm$-$the range most commonly used in remote sensing of the earth's atmosphere. Also, shown are the results for a model ash cloud with mean particle radii of 1 and 5 μm.

Table 3: Optical parameters for a model andesite ash cloud. The parameters are: ϖ–the single-scatter albedo, g– the asymmetry parameter, and Q_{ext}–the extinction efficiency factor. These parameters are given for three mean particle sizes, r_o=1, 3 and 5 μm.

	r_o=1.0 μm			r_o=3.0 μm			r_o=5.0 μm		
Wavelength (μm)	ϖ	g	Q_{ext}	ϖ	g	Q_{ext}	ϖ	g	Q_{ext}
0.30	0.8346	0.4579	2.0875	0.8344	0.4573	2.0873	0.8343	0.4570	2.0872
0.32	0.8241	0.4551	2.0875	0.8238	0.4543	2.0873	0.8237	0.4540	2.0872
0.34	0.8229	0.4548	2.0876	0.8225	0.4540	2.0873	0.8224	0.4536	2.0872
0.36	0.8104	0.4513	2.0876	0.8100	0.4503	2.0873	0.8098	0.4499	2.0872
0.38	0.8105	0.4515	2.0877	0.8100	0.4504	2.0873	0.8098	0.4499	2.0872
0.40	0.7987	0.4480	2.0877	0.7982	0.4467	2.0873	0.7980	0.4462	2.0872
0.42	0.7988	0.4482	2.0878	0.7982	0.4469	2.0874	0.7980	0.4462	2.0872
0.44	0.7877	0.4448	2.0879	0.7871	0.4433	2.0874	0.7868	0.4426	2.0872
0.46	0.7878	0.4451	2.0880	0.7871	0.4434	2.0874	0.7868	0.4427	2.0872
0.48	0.7879	0.4454	2.0880	0.7872	0.4436	2.0875	0.7868	0.4428	2.0872
0.50	0.7775	0.4421	2.0881	0.7766	0.4401	2.0875	0.7762	0.4392	2.0872
0.52	0.7776	0.4424	2.0882	0.7767	0.4403	2.0876	0.7763	0.4393	2.0872
0.54	0.7778	0.4428	2.0883	0.7768	0.4405	2.0876	0.7763	0.4394	2.0873
0.56	0.7679	0.4396	2.0884	0.7668	0.4371	2.0876	0.7663	0.4359	2.0873
0.58	0.7681	0.4400	2.0886	0.7669	0.4373	2.0877	0.7663	0.4361	2.0873
0.60	0.7683	0.4405	2.0887	0.7670	0.4376	2.0878	0.7664	0.4362	2.0874
0.70	0.7509	0.4363	2.0894	0.7490	0.4321	2.0881	0.7482	0.4302	2.0875
0.80	0.7357	0.4331	2.0903	0.7331	0.4274	2.0886	0.7320	0.4248	2.0878
0.90	0.7225	0.4313	2.0914	0.7191	0.4236	2.0892	0.7176	0.4202	2.0882
1.00	0.7112	0.4308	2.0928	0.7067	0.4209	2.0899	0.7048	0.4165	2.0887
1.10	0.7016	0.4319	2.0945	0.6960	0.4192	2.0908	0.6935	0.4136	2.0892
1.20	0.6937	0.4346	2.0966	0.6866	0.4186	2.0918	0.6836	0.4118	2.0899
1.30	0.6873	0.4392	2.0991	0.6786	0.4193	2.0931	0.6749	0.4109	2.0908
1.40	0.6871	0.4476	2.1021	0.6763	0.4234	2.0945	0.6720	0.4132	2.0917
1.50	0.6834	0.4562	2.1057	0.6702	0.4266	2.0963	0.6651	0.4144	2.0929
1.60	0.6853	0.4685	2.1101	0.6694	0.4331	2.0983	0.6632	0.4185	2.0942
1.70	0.6883	0.4830	2.1155	0.6691	0.4408	2.1007	0.6619	0.4236	2.0957
1.80	0.6926	0.4998	2.1219	0.6695	0.4499	2.1034	0.6610	0.4298	2.0975
1.90	0.6983	0.5189	2.1298	0.6706	0.4605	2.1066	0.6607	0.4371	2.0995
2.00	0.7019	0.5411	2.1395	0.6688	0.4728	2.1104	0.6572	0.4454	2.1019
2.10	0.7143	0.5655	2.1511	0.6749	0.4880	2.1148	0.6614	0.4565	2.1046
2.20	0.7248	0.5909	2.1651	0.6785	0.5038	2.1199	0.6627	0.4677	2.1076
2.30	0.7369	0.6174	2.1817	0.6829	0.5213	2.1258	0.6647	0.4803	2.1110
2.40	0.7507	0.6441	2.2014	0.6882	0.5406	2.1326	0.6672	0.4944	2.1150
2.50	0.7686	0.6699	2.2242	0.6977	0.5621	2.1404	0.6736	0.5109	2.1195
2.55	0.7750	0.6821	2.2369	0.6996	0.5727	2.1448	0.6739	0.5188	2.1219
2.60	0.7845	0.6935	2.2503	0.7049	0.5843	2.1494	0.6775	0.5279	2.1245
2.65	0.7885	0.7045	2.2645	0.7043	0.5953	2.1544	0.6752	0.5361	2.1273
2.70	0.7955	0.7145	2.2795	0.7072	0.6070	2.1597	0.6762	0.5453	2.1302
2.75	0.7931	0.7249	2.2949	0.6996	0.6183	2.1653	0.6670	0.5533	2.1333
2.80	0.7961	0.7338	2.3110	0.6983	0.6306	2.1712	0.6639	0.5630	2.1366
2.85	0.8037	0.7407	2.3277	0.7022	0.6432	2.1776	0.6659	0.5738	2.1401
2.90	0.8091	0.7468	2.3448	0.7040	0.6559	2.1843	0.6658	0.5847	2.1437
2.95	0.8185	0.7507	2.3623	0.7106	0.6682	2.1914	0.6703	0.5963	2.1476
3.00	0.8275	0.7534	2.3800	0.7173	0.6802	2.1988	0.6750	0.6080	2.1517
3.05	0.8381	0.7545	2.3980	0.7265	0.6917	2.2067	0.6821	0.6198	2.1560
3.10	0.8464	0.7549	2.4158	0.7334	0.7028	2.2149	0.6871	0.6316	2.1605
3.15	0.8543	0.7544	2.4335	0.7404	0.7133	2.2235	0.6923	0.6433	2.1653
3.20	0.8635	0.7526	2.4511	0.7498	0.7229	2.2324	0.7000	0.6550	2.1702
3.25	0.8688	0.7511	2.4682	0.7546	0.7325	2.2416	0.7030	0.6666	2.1754
3.30	0.8739	0.7489	2.4848	0.7593	0.7414	2.2512	0.7062	0.6781	2.1807
3.35	0.8803	0.7458	2.5009	0.7664	0.7491	2.2611	0.7118	0.6892	2.1863
3.40	0.8862	0.7423	2.5163	0.7733	0.7560	2.2713	0.7174	0.7000	2.1920
3.45	0.8904	0.7390	2.5308	0.7779	0.7625	2.2817	0.7208	0.7107	2.1980
3.50	0.8943	0.7355	2.5444	0.7825	0.7682	2.2924	0.7242	0.7210	2.2041
3.60	0.9014	0.7281	2.5686	0.7915	0.7773	2.3146	0.7312	0.7403	2.2168
3.70	0.9101	0.7198	2.5882	0.8041	0.7821	2.3376	0.7427	0.7565	2.2302
3.80	0.9166	0.7120	2.6023	0.8140	0.7846	2.3614	0.7518	0.7706	2.2442
3.90	0.9233	0.7042	2.6105	0.8252	0.7842	2.3859	0.7628	0.7815	2.2586
4.00	0.9277	0.7108	2.5773	0.8341	0.7921	2.4195	0.7706	0.7975	2.2773
4.25	0.9352	0.6941	2.5293	0.8494	0.7846	2.4868	0.7858	0.8109	2.3174
4.50	0.9402	0.6765	2.4326	0.8623	0.7737	2.5565	0.7991	0.8122	2.3595
4.75	0.9432	0.6564	2.2915	0.8733	0.7630	2.6272	0.8107	0.8060	2.4037
5.00	0.9413	0.6419	1.9900	0.8819	0.7704	2.6963	0.8184	0.8058	2.4602
5.25	0.9389	0.6130	1.7826	0.8875	0.7668	2.7580	0.8242	0.7977	2.5105
5.50	0.9363	0.5811	1.5711	0.8942	0.7646	2.8121	0.8322	0.7894	2.5637
5.75	0.9300	0.5473	1.3668	0.8966	0.7648	2.8536	0.8351	0.7841	2.6194
6.00	0.9101	0.5133	0.9693	0.9004	0.7970	2.7883	0.8464	0.8093	2.7209
6.50	0.8380	0.4382	0.5776	0.8790	0.8161	2.5113	0.8356	0.8449	2.8205
7.00	0.6549	0.3645	0.3470	0.8058	0.8202	1.9370	0.7889	0.8848	2.6700
7.50	0.3096	0.2950	0.2404	0.5937	0.8105	1.1636	0.6491	0.9068	1.9243
8.00	0.0625	0.2346	0.2882	0.2155	0.7863	0.8026	0.3052	0.9043	1.1673
8.25	0.0655	0.2090	0.4060	0.2279	0.7644	0.9701	0.3203	0.8907	1.3045
8.50	0.1075	0.1876	0.6204	0.3284	0.7318	1.3266	0.4219	0.8611	1.6615
8.75	0.1541	0.1706	1.0082	0.4087	0.6886	1.7910	0.4909	0.8110	2.0317
9.00	0.2049	0.1552	1.7692	0.4686	0.6440	2.3946	0.5405	0.7500	2.4372
9.50	0.1948	0.1366	1.7248	0.4238	0.6592	2.5902	0.4845	0.7775	2.5805
10.00	0.2305	0.1146	1.7813	0.4522	0.6202	2.8094	0.5021	0.7457	2.7180
10.50	0.2495	0.1181	1.3480	0.4546	0.6133	2.8707	0.4883	0.7495	2.7459
11.00	0.3553	0.1286	0.8027	0.5088	0.5991	3.1600	0.4782	0.7452	2.8292
11.50	0.4019	0.0997	0.4043	0.6265	0.5784	3.2195	0.5362	0.7079	3.0643
12.00	0.3958	0.0778	0.2422	0.6997	0.5613	2.8904	0.6367	0.6834	3.3369
12.50	0.3572	0.0625	0.1627	0.7302	0.5433	2.4190	0.7080	0.6870	3.4567
13.00	0.2762	0.0515	0.1285	0.7139	0.5216	1.9619	0.7268	0.7007	3.3357
13.50	0.1904	0.0433	0.1110	0.6736	0.4931	1.5435	0.7210	0.7084	3.0193
14.00	0.1153	0.0377	0.1134	0.5966	0.4607	1.2558	0.6783	0.7107	2.6238

6 Cloud height determination

Cloud-top temperature/temperature profile method

Cloud-top height can be determined by using the cloud-top temperature of opaque parts of the cloud as a proxy for the ambient temperature at the same height as the cloud top. A nearby radiosonde profile is then used to determine the height in the profile where the temperature best matches the cloud-top temperature. This method can work well provided the cloud behaves as a blackbody and the radiosonde profile is representative. For high clouds near the tropopause, the method is prone to error because the rate of change of temperature with height is small and this leads to indeterminacy in the height assignment.

Figure 6 shows an AVHRR-2 image of the volcanic ash plume on 17 June 1996. The plume is shown as the 11 μm brightness temperature (AVHRR-2 channel 4) overlayed on the near infrared (AVHRR-2 channel 2) image. The plume was highlighted by selecting only those regions for which $T_4 - T_5 < +0.5$ K. The coldest parts of the plume (coloured blue) have temperatures in the range -32 °C to -38 °C. It is reasonable to expect that the cloud is not black (see, for example Platt and Stephens, 1984), so the air temperature at the top of the cloud might be expected to be a few K lower. The four locations marked on the image correspond to thick cloud cloud (A), semi-transparent cloud (B), clear sea surface (C), and clear land surface (D). The 11 μm brightness temperatures corresponding to these locations are: -37 °C (A), -4.2 °C (B), 12.8 °C (C), and 7.3 °C (D).

Radiosonde data were obtained from the Crown Research Institute, New Zealand (Burgess, personal communication) for two upper air stations at Whenauapi (36.47 °S, 174.38 °E) and Paraparaumu (40.54 °S, 174.59 °E). Launches were made at approximately 0000 UTC and 1200 UTC on 17 June 1996. Figure 7 shows the vertical temperature profiles at Whenauapi locations at $\tilde{0}000$ and $\tilde{1}200$ UTC, 17 June. The vertical dotted lines on the plot indicate temperatures of -35 °C and -45 °C, which cover the range of opaque cloud top temperatures observed in the AVHRR image. These temperatures translate to heights of 7.5 to 8.5 km. Radiosonde data at Paraparaumu and data for the other days, give substantially the same results. Indeed it is sufficient to use the mean monthly profiles in this analysis, because the lapse rate is not varying strongly during this time in this height range of the atmosphere. (Note that this may not have been the case had the plume been higher, or lower, in the atmosphere.)

The plumes of 8 July observed in ATSR-2 and in AVHRR-2 imagery indicate that in the most opaque regions, the coldest parts of the cloud were -20 °C to -25 °C. These temperatures translate to cloud top heights of about 5 to 6 km.

Cloud stereoscopy

Prata and Turner (1997) have developed an algorithm for determining cloud heights from the parallax formed between the ATSR forward and nadir views of clouds. The method is capable

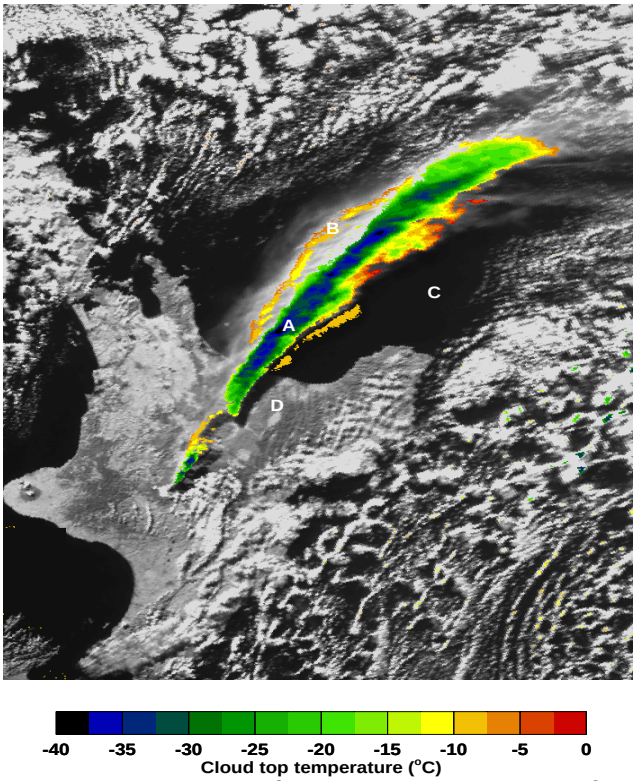

Figure 6. Brightness temperature (T_4) for the Ruapehu plume of 17 June 1996.

of accuracies of $\approx$ 1 km in height and was used to determine plume height in the ATSR-2 image of 8 July. Figure 8 shows the plume at nadir (Fig. 8a) and in the forward view (Fig. 8b), using the 1.61 μm channel. A point on the plume some distance downwind of the vent (marked by + on the Figures) and a point on the plume near to the vent (marked by **X** on the Figures) are used to illustrate the results. It is apparent that the same points are shifted by several lines in the forward view relative to the nadir view. For the points shown, the stereoscopic retrieval gives heights of $\approx$ 7 km for the downwind point, and 5.5 km for the point near to the vent (cf. heights of 5-6 km from the brightness temperature method). Height retrievals along the length of the plume suggest a slight rise of the plume from about 5 km near to the vent to about 8 km downwind.

Height from plume shadow

The AVHRR-2 image of 17 June lends itself to a determination of plume height morphology from the shadow cast on the underlying surface. The method used to determine the plume height is applied separately for portions over the sea and over the land. We describe the analysis for deriving the plume height from the image of the plume and its shadow. The case of the shadow on the ocean is described first, then the more complicated case for the land.

Figure 9 shows the geometry when the shadow falls on the flat ocean. Define an x-y coordinate

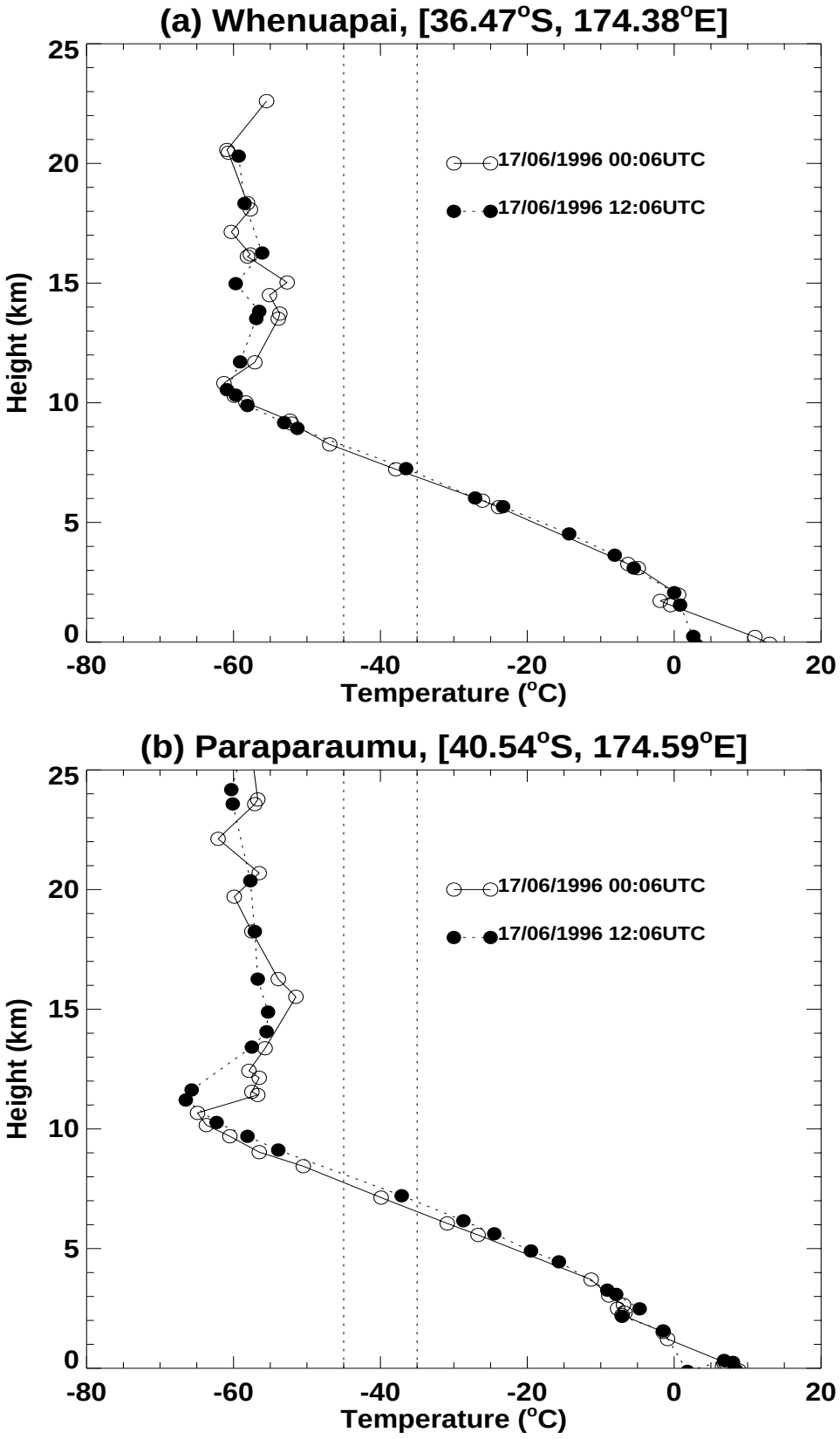

Figure 7. Radiosonde profiles.

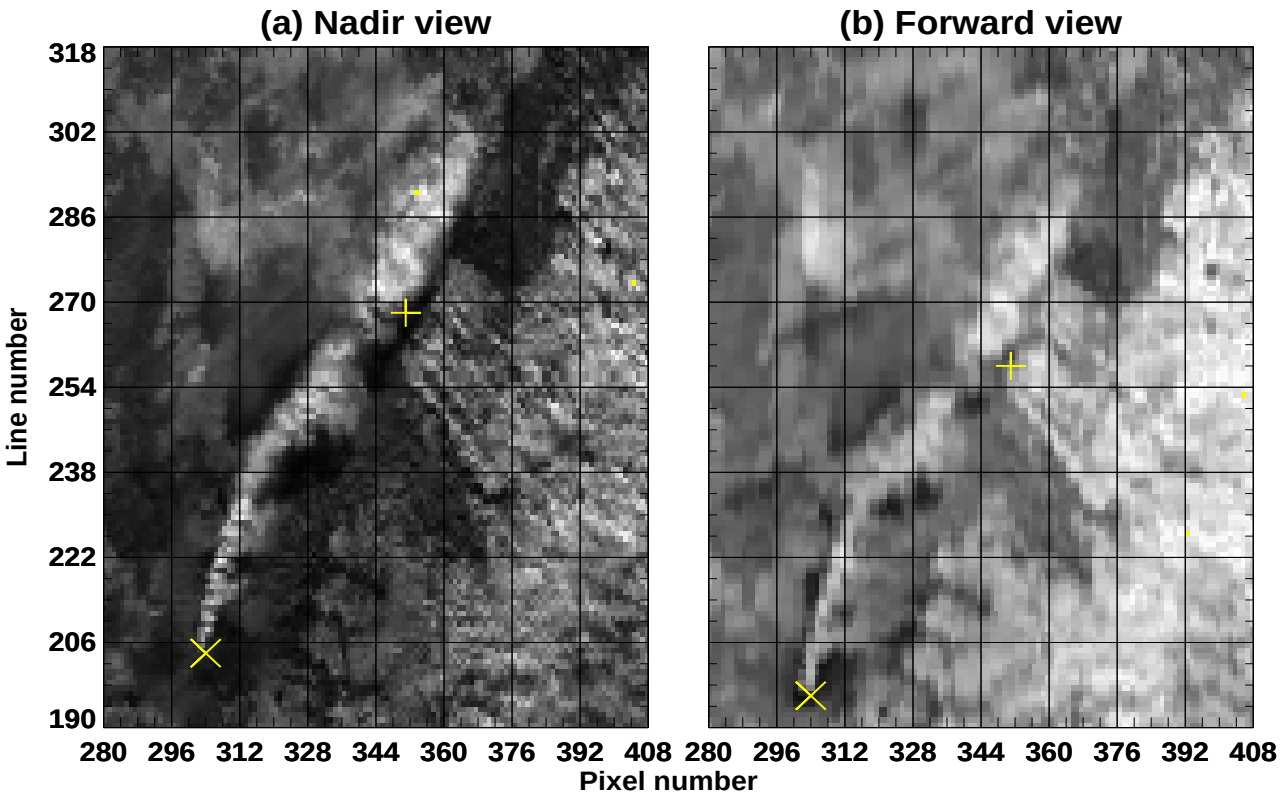

Figure 8. ATSR-2 stereoscopy. The *left panel* shows the nadir view of a portion of the Ruapehu plume. The *right panel* shows the corresponding plume in the forward view. Two points marked **X** and **+** are displaced in the forward view with respect to the nadir view.

system on the ocean surface with x north and y east, and consider a point T on the plume edge at altitude h above the origin. The direction of the satellite from T is described by the zenith angle θ and the azimuth ϕ, and the solar direction is given by angles θ_0 and ϕ_0. Point T casts its shadow at point S on the surface, and the position of T in the image is actually that of its projection P along the satellite view direction to the surface. S and P have coordinates

$$\begin{aligned} x_S &= h\ \tan\theta_0\ \cos(\phi_0 - \pi) \\ y_S &= h\ \tan\theta_0\ \sin(\phi_0 - \pi) \\ x_P &= h\ \tan\theta\ \cos(\phi - \pi) \\ y_P &= h\ \tan\theta\ \sin(\phi - \pi). \end{aligned} \tag{12}$$

The vector $\mathbf{\Delta}$ from P to S has components

$$\begin{aligned} x_{\mathbf{\Delta}} &= hX \\ y_{\mathbf{\Delta}} &= hY, \end{aligned} \tag{13}$$

where

$$\begin{aligned} X &= \cos\phi\ \tan\theta - \cos\phi_0\ \tan\theta_0 \\ Y &= \sin\phi\ \tan\theta - \sin\phi_0\ \tan\theta_0. \end{aligned} \tag{14}$$

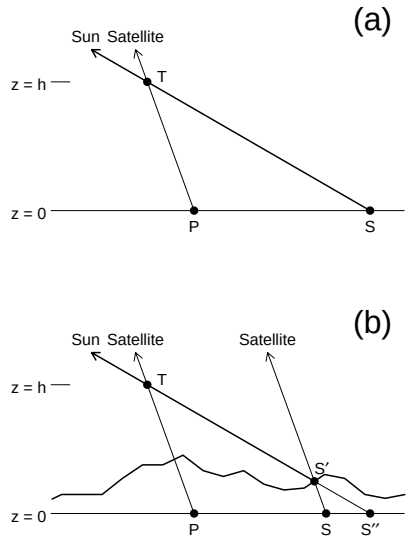

Figure 9. *(a)* The geometry over the ocean for a case where the view and sun directions are in the same vertical plane, depicted in that plane. *(b)* The geometry with the view and sun angles as in panel (a), but now over land.

The direction of $\mathbf{\Delta}$ is described by its azimuth

$$\phi_{\mathbf{\Delta}} = \arctan \frac{Y}{X}, \tag{15}$$

and its magnitude is

$$d = h\sqrt{X^2 + Y^2}. \tag{16}$$

Because $\phi_{\mathbf{\Delta}}$ is independent of h, the association between points on the plume edge and points on the shadow edge in the image is straightforward; any point on the imaged plume edge is connected to its shadow point by a line with orientation $\phi_{\mathbf{\Delta}}$. The true height of the plume edge is proportional to the separation of the plume and shadow edges along this line,

$$h = \frac{d}{\sqrt{X^2 + Y^2}}. \tag{17}$$

The analysis of the shadow on the ocean begins by rotating the image so that, for example, the y-direction is parallel to the azimuth $\phi_{\mathbf{\Delta}}$. Then each column in the image is analyzed separately; the edge points of the plume and shadow images are found, then the relative three-dimensional coordinates of the true plume edge point determined by equations (17) and (13). At first we tried to set the plume and shadow edges at the local extrema of $d(\log r)/dy$, where r is the pixel radiance, but these positions were somewhat unstable, fluctuating along the plume.

Instead we used a constant radiance contour, set at the median of the radiance at the extremum of $d(\log r)/dy$ along the analyzed portion of the plume. When the shadow falls on land, the topography introduces additional complexity. Figure 9(a) shows the essential features of the ocean geometry with a simplified case in which the view and sun direction lie in the same vertical plane. A point T on the true plume edge appears in the satellite image at the point P on the surface, which is the projection of T along the view direction; the shadow of T appears at point S on the surface, which is the projection of T along the sun direction. Once the positions

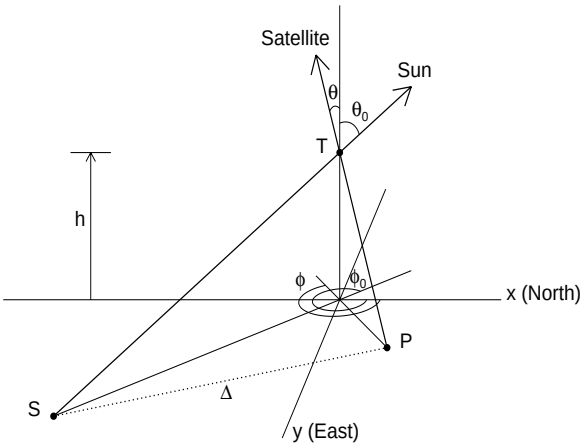

Figure 10. The geometry of the image and shadow of a point on the plume edge in the case where the shadow falls on the ocean.

of P and S in the image are determined, it is the rays $\vec{ST}$ and $\vec{PT}$ that fix the location of T. Figure 9(b) shows the situation on land. Because the geolocation of the AVHRR image treats all image features as being at zero altitude, T still appears in the image at location P on the zero-altitude surface. However, the shadow of T is now on the land surface at S', and appears in the image at the projection of S' along the view direction to the point S on the zero-altitude surface. Point S' can be determined by projecting S upwards along the view direction to intersect the ground surface as represented by a digital elevation model (DEM). Then the rays $\vec{S'T}$ and $\vec{PT}$ fix T. A plume edge is treated as a set of many points $\{T_i\}$, which generates sets of points $\{S_i\}$, $\{P_i\}$. In a three-dimensional situation more typical than that shown in Fig. 9, it is not clear *a priori* which points in $\{S_i\}$ and $\{P_i\}$ are associated, through the same point T. However, if each point S' is projected along the sun direction down to S'' on the zero-altitude surface, then the analytic ocean method applies, corresponding points P and S'' being joined by lines of azimuth $\phi_{\mathbf{\Delta}}$ So over land the procedure is to determine the edge points P and S, project S up to S' on the DEM, project S' down to S'', rotate so that the y-axis lies at azimuth $\phi_{\mathbf{\Delta}}$ and for points P and S'' with the same x-coordinate use the equations above to locate T.

The analysis presented in this paper used a constant value for $\phi_{\mathbf{\Delta}}$ of 153° over the ocean and 149° over the land. Channels 1 and 2 were used for the ocean and land analyses, respectively. The radiance contours delineating the plume and shadow edges in the image were set as described above, except that for the shadow edge on land the contour level was raised slightly to handle the shadow being less dark near $x \simeq 260$ km in Figure 11. The DEM used was the National Geophysical Data Center Terrain Base Global Digital Terrain Model Version 1.0

(available at http://www.ngdc.noaa.gov/mgg/global/seltopo.html), which has 5-arcminute resolution.

Figure 11 shows a close-up channel 1 (visible) view of a part of the AVHRR-2 image of the Mt. Ruapehu plume obtained on 17 June 1996. Where the plume crosses the North Island of New Zealand there is a distinct darkening of the channel 1 reflectance. This shadow can also be detected over the ocean when the image data are suitably enhanced. Since time and position of each pixel are available it is straightforward to obtain the relevant solar and satellite viewing angles required to compute the height of the illuminated edge of the plume. The morphology of real plumes is likely to be quite complex and it is difficult to calculate the precise part of the cloud that is responsible for the shadow.

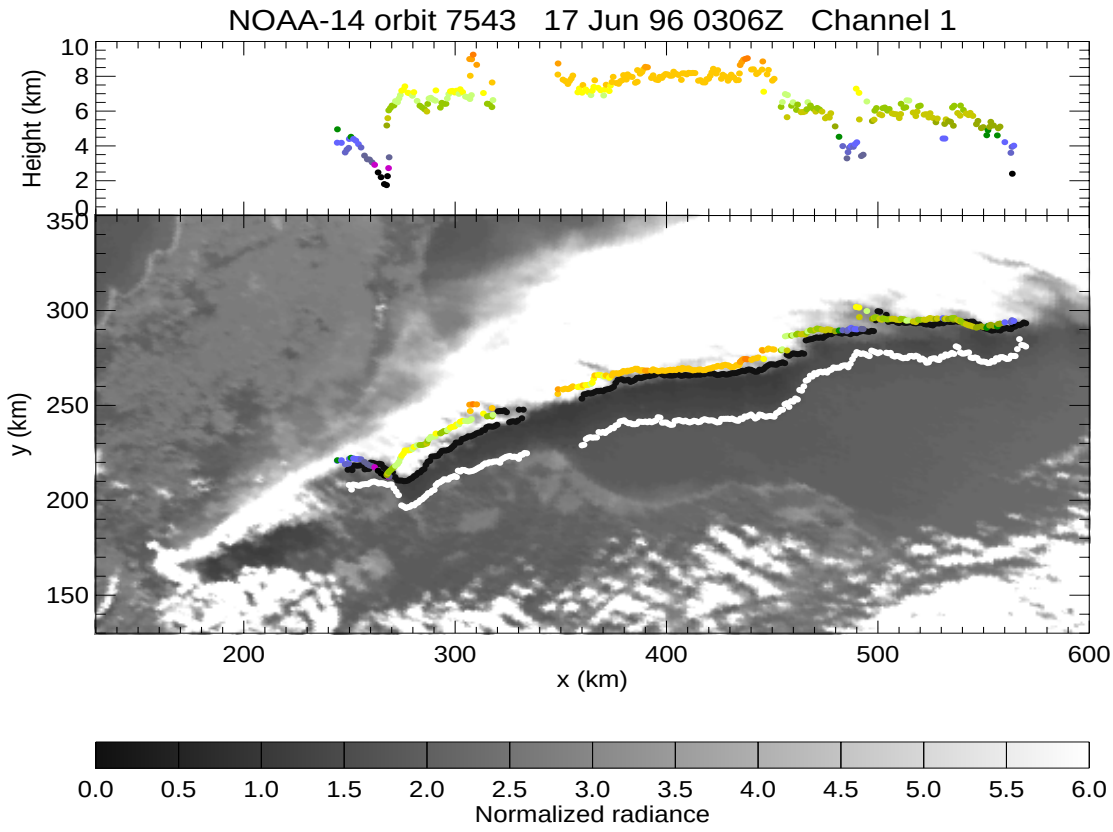

Figure 11. *Bottom panel:* The AVHRR channel 1 image, rotated so that the y-axis is in the azimuth $\phi_{\Delta} = 153^{\circ}$ described in the text. The black points are taken as the plume edge (points P in the appendix) and the white points as the shadow edge (points S). The coloured points show the vertical projection of the calculated true plume edge; that is, the plume edge where it would be imaged by a nadir-viewing satellite. The colours code the calculated height of the plume edge and represent the same height intervals as in the top panel. *Top panel:* The calculated height of the plume edge.

Figure 11 also shows the retrieval of height of the plume edge (top panel) and corresponding locations of the edge and its shadow as determined on the AVHRR-2 image. As described previously, the height retrieved by this method is, strictly speaking, that of the plume edge

(Glaze *et al.*, 1999). We expect this height to correspond more closely with the lower part of the plume, and represent a lower bound on the plume height and an upper bound on the plume base. The plume edge height varies from values as small as 2 km, up to just over 8 km, some 200 km downwind of the vent.

7 Water vapour corrections

Water vapour has a differential absorption effect on the infrared window radiances so that at the top of the atmosphere the radiance (or brightness temperature) is larger at 11 μm than at 12 μm. This is the opposite to the absorption effect caused by volcanic ash and thus water vapour can 'hide' the ash effect. A method to correct for the water vapour effect, based on global radiative transfer simulations has been devised and is described here.

Global radiative transfer calculations

Detailed radiative transfer calculations were performed using the MODTRAN-3 code to determine the top-of-the-atmosphere (TOA) brightness temperatures for the AVHRR, GMS-5, GLI and ATSR-2 split-window channels. The calculations utilised global NCEP analyses for four different days and two different times. The days and times were chosen to represent seasonal and diurnal variations in atmospheric water vapour conditions. Figure 12 shows the TOA brightness temperature at 11 μm (top panel), the precipitable water amount (cm), and the temperature difference ($T_4 - T_5$) between the 11 μm and 12 μm AVHRR split window channels. The calculations shown are for 26 December 1996 at 00Z. The most notable feature of these calculations is the high degree of spatial correlation between the fields of precipitable water and $T_4 - T_5$. There is a marked nonlinear relationship between the TOA brightness temperature and precipitable water. Similar results were found for the other days and times.

Water vapour amount is not distributed uniformly over the globe. Largest amounts are found in tropical and subtropical regions while the polar regions are relatively dry. Water vapour distributions also appear to follow weather systems and the patterns resemble the cloud patterns associated with frontal systems. There also appears to be a strong correlation between warm ocean current systems and high water vapour loadings. These general patterns in water vapour amount (or precipitable water) are reflected in the global patterns of AVHRR T_4-T_5.

Results for the GMS-5, ATSR-2 and GLI are shown for comparison in the panels of Figure 13. There are minor differences between $T_4 - T_5$ for the ATSR-2, GLI and AVHRR sensors, but major differences for the GMS-5 sensor. This is essentially due to the degree of overlap between the GMS-5 split window channels, which reduces the size of the $T_4 - T_5$ difference for a given precipitable water amount.

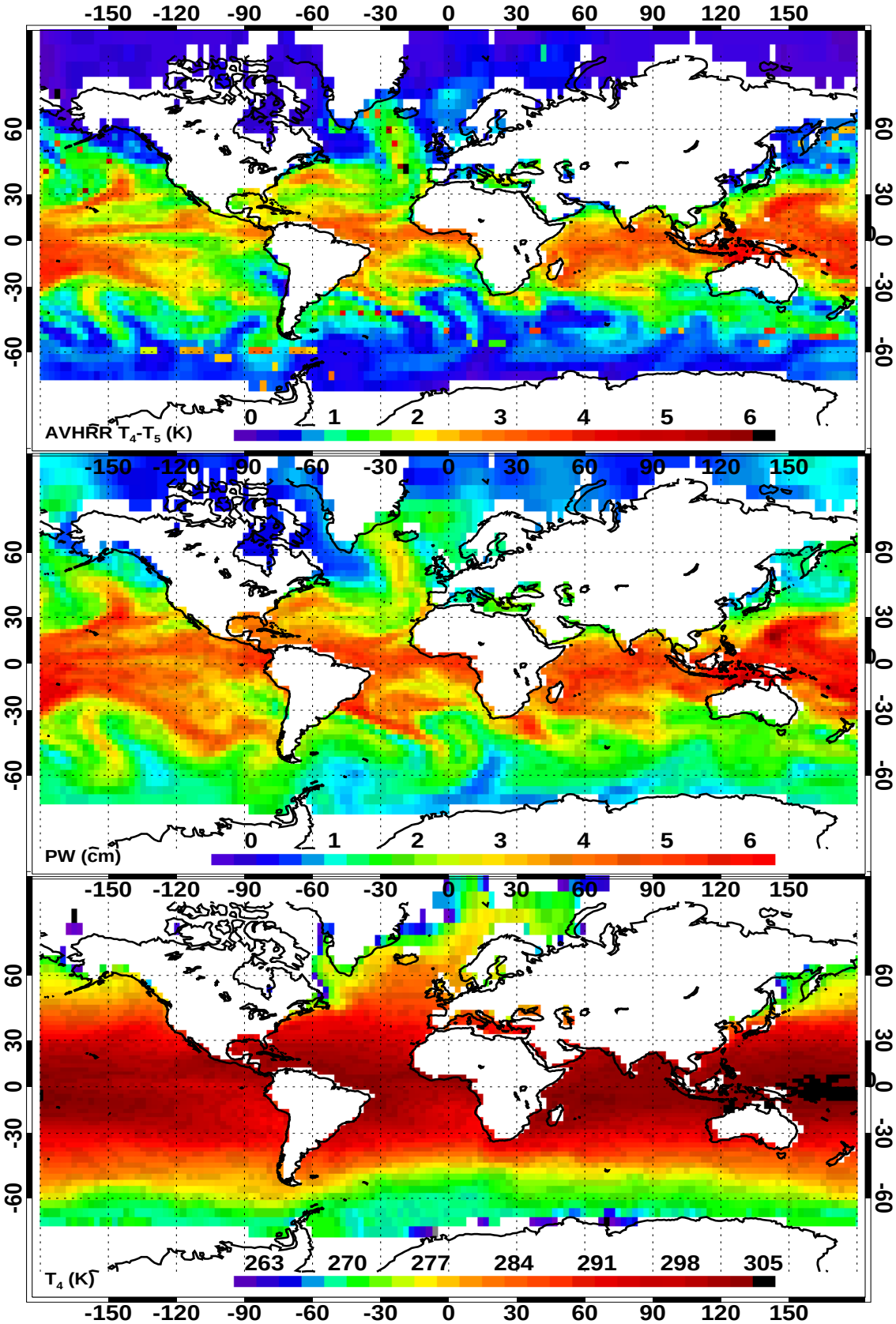

Figure 12. Global distributions of 11 μm - 12 μm brightness temperatures (T_4-T_5, K; top panel) precipitable water (cm; middle panel) and 11 μm brightness temperature (K; bottom panel) for 26 December 1996 at 00 Z.

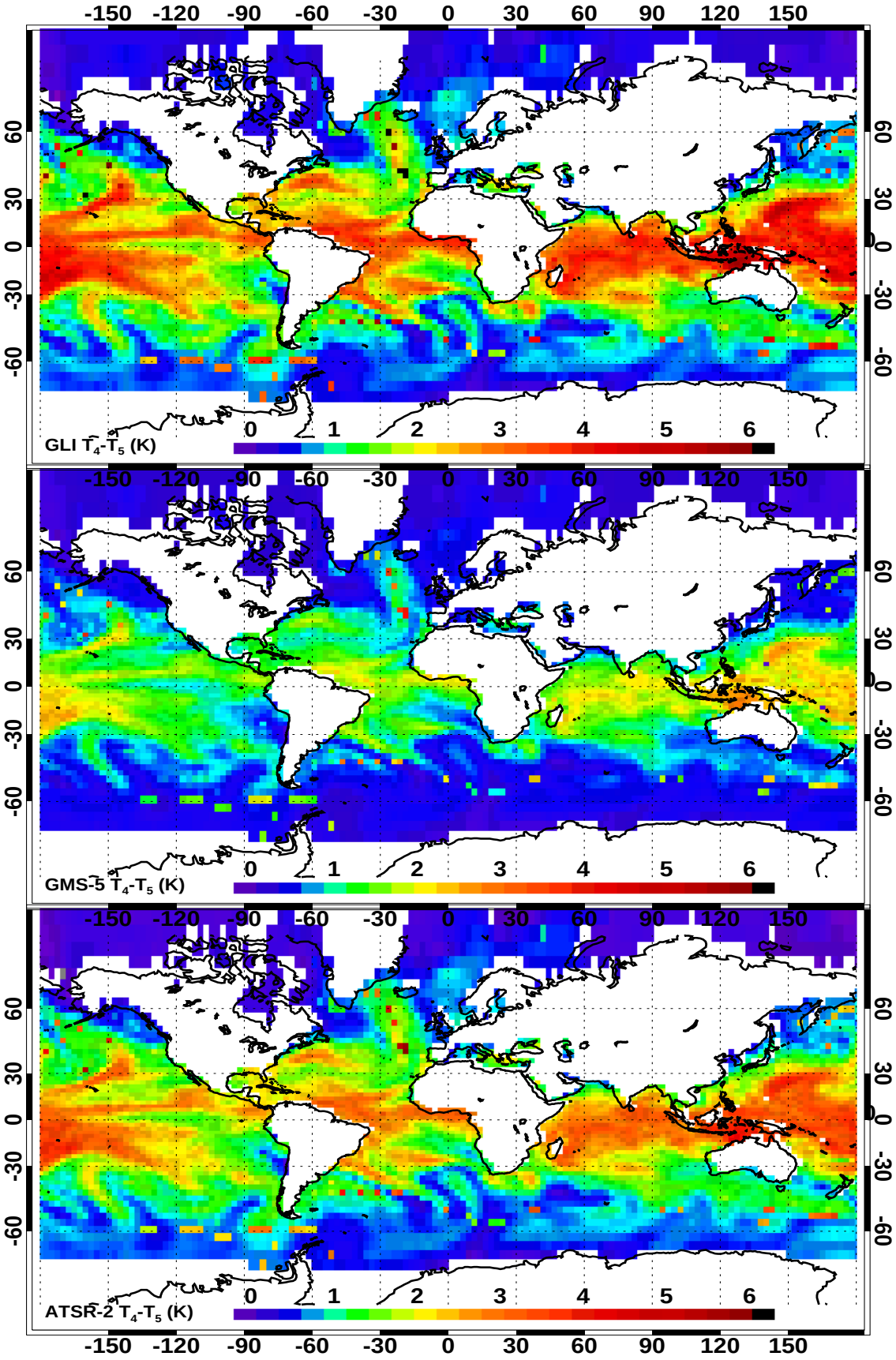

Figure 13. Global distributions of GLI 11 μm - 12 μm brightness temperatures (T_4-T_5, K; top panel) GMS-5 (K; middle panel) and ATSR-2 (K; bottom panel) for 26 December 1996 at 00 Z.

A semi-empirical water vapour correction

The RT calculations suggest that there is a very strong correlation between precipitable water and $T_4 - T_5$ and a strong, but nonlinear correlation between precipitable water and top-of-the-atmosphere temperature at 11 μm or 12 μm. This latter nonlinear relation derives from the correlation between SST and precipitable water. Therefore there exists a nonlinear correlation between $T_4 - T_5$ and T_4 through precipitable water. This fact is no surprise as it is the basis for estimating SST from the AVHRR and other instruments relying on the split-window channels.

Figure 14 shows the correlations between precipitable water (in cm) and $T_4 - T_5$, and T_4 and $T_4 - T_5$ calculated using RT and the NCEP data described earlier.

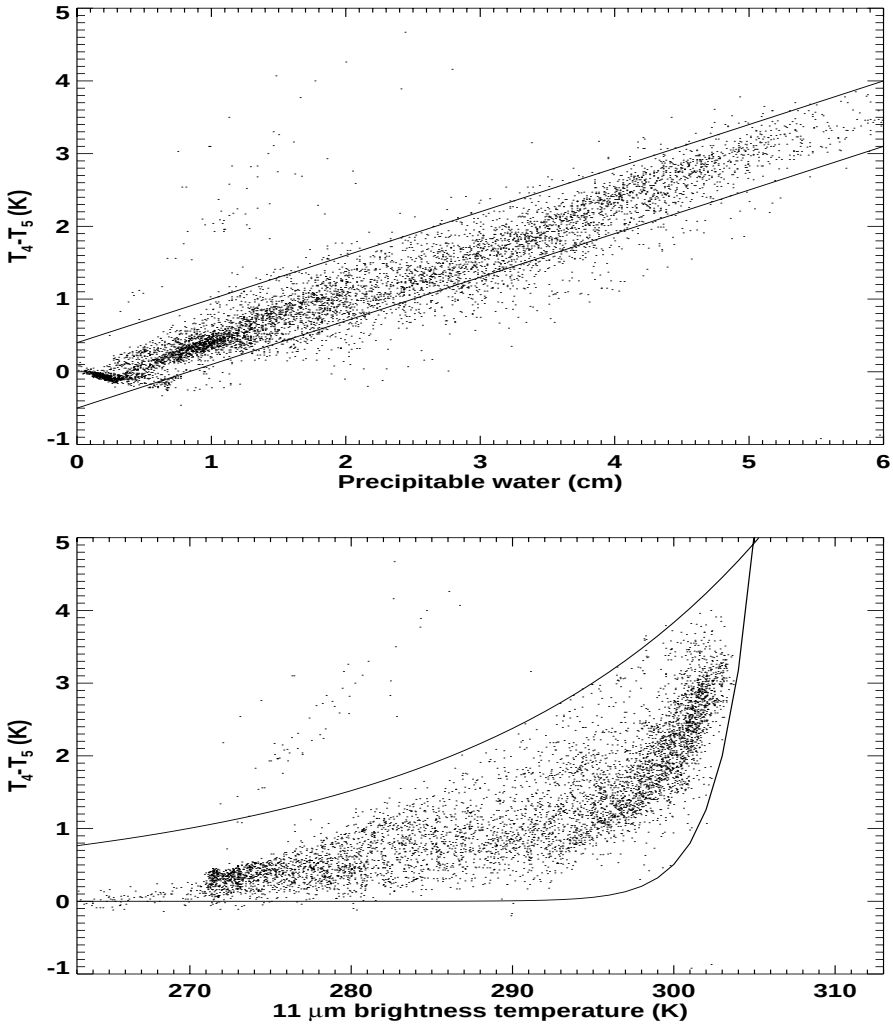

Figure 14. Global distributions of 11 μm - 12 μm brightness temperatures (T_4-T_5, K; top panel) precipitable water (cm; middle panel) and 11 μm brightness temperature (K; bottom panel) for 26 December 1996 at 00 Z.

The data shown are for 26-12-1996 at 00Z, but very similar results are obtained for other dates and times. Also shown on Figure 12 are empirical fits providing upper and lower bounds to the distribution of the points. The semi-empirical relations describing these bounds are,
Upper bound:

$$\Delta T_{wv} = \exp\left[20T_* - 18\right]. \tag{18}$$

Lower bound:

$$\Delta T_{wv} = \exp\left[6T_* - b\right], \tag{19}$$

where $T_* = T_4/T_{max}$, and T_{max} is an arbitrary normalisation constant assigned a value of 320 K. The free parameter b essentially determines the value of the water vapour effect on $T_4 - T_5$ at the maximum value of T_4. Hence b can be determined directly from the image data, allowing realistic flexibility on the size of the water vapour correction determined by this semi-empirical approach.

Test case: Rindjani eruptions, Indonesia, June 1994

The semi-empirical approach to water vapour correction for volcanic ash detection has been tested on some eruptions of Rindjani volcano on the island of Lombok in Indonesia. These eruptions were mostly low level and occurred in a moisture laden, tropical atmosphere. Detection using the reverse absorption effect was successful on many AVHRR images, but it is known from the work of Prata (1989a, b), Wen and Rose (1994), and Davies and Rose (1998) that water vapour will have the effect of suppressing the size of the negative differences. Thus a water vapour correction is warranted. Four test cases are shown in Figure 15, where distributions of $T_4 - T_5$ vs. T_4 are plotted without a water vapour correction (black points), and with a water vapour correction (red points).

The continuous line is a simplified model of the behaviour of ΔT for volcanic ash clouds described by Prata and Grant (2000) and developed from radiative transfer considerations. The model may be written:

$$\Delta T = \Delta T_s[X - X^\beta], \tag{20}$$

where,

$$X = 1 - \frac{\Delta T_s}{\Delta T_4},$$

$$\Delta T_4 = T_4 - T_c,$$

$$\Delta T_s = T_s - T_c,$$

and the cloud-top and surface temperatures are T_c and T_s. The parameter β links the spectral behaviour of the top-of-the atmosphere brightness temperatures (T_4, T_5) to the cloud microphysics, through the ratio of spectral extinction efficiencies for volcanic ash. Mie calculations by Prata (1989b) and Prata and Barton (1994) for silicate spherical particles suggest values of β from $\approx$ 0.6 to $\approx$ 0.86. A value of β=0.71 was used in Figure 15.

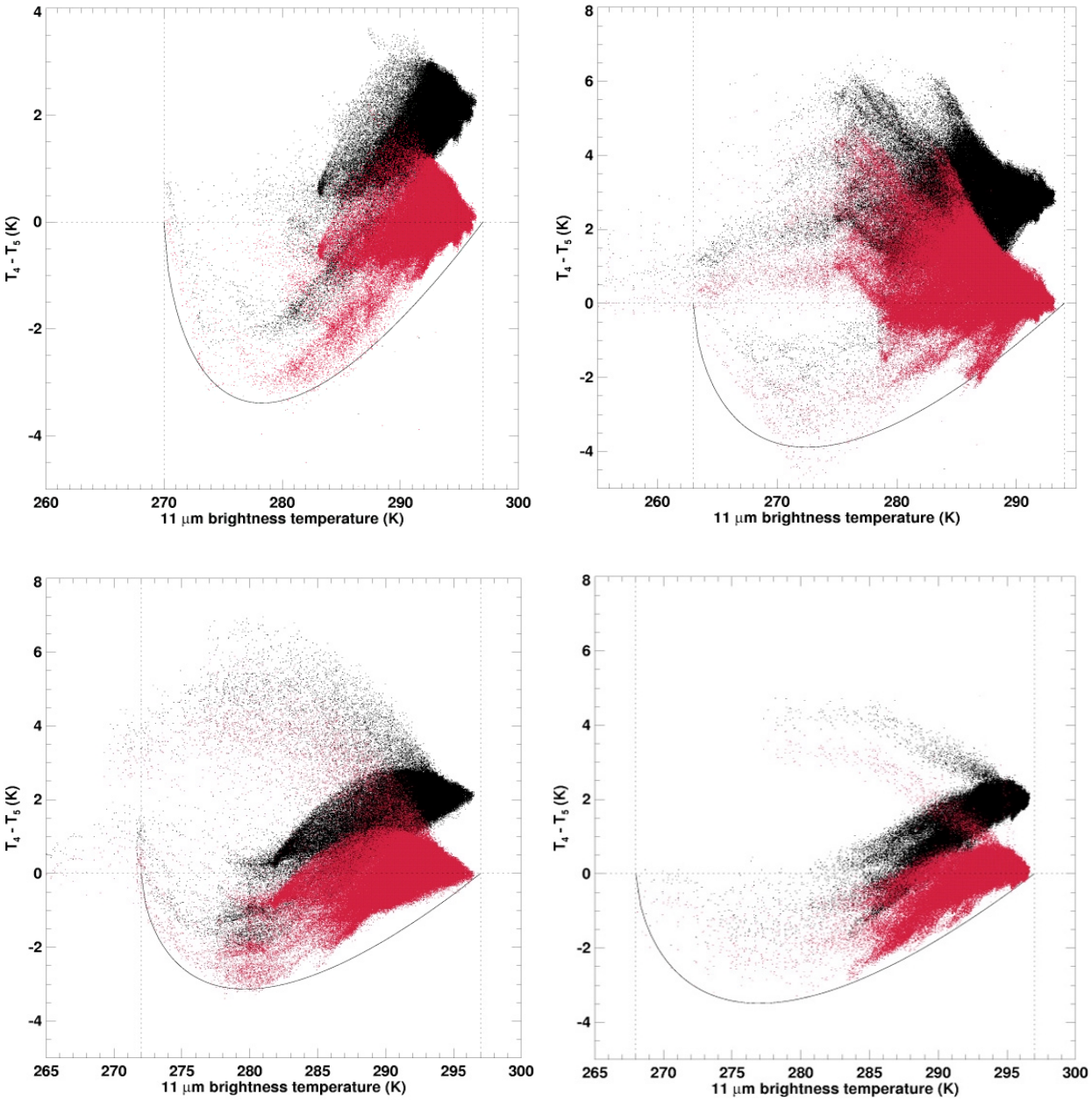

Figure 15. Temperature difference distributions without (black dots) and with (red dots) a water vapour correction for four different eruption clouds from Rindjani, Indonesia.

Theory suggests values of $\Delta T < 0$ are ash, but this does not take into account measurement errors, primarily resulting from instrument noise, poor calibration and channel misregistration. The water vapour correction and the theory utilised are also approximations and contain some degree of uncertainty. Each pixel is likely to contain a mixture of water vapour and ash. We assume that the temperature difference observed arises from a linear combination of the signal from ash (ΔT_{ash}) and the signal from an otherwise clear pixel, any temperature difference being due to water vapour (ΔT_{wv}). If the fraction of ash in the mixture is F, then we may write the observed temperature difference as,

$$\Delta T = F \Delta T_s [Z - Z^{\beta}], \tag{21}$$

where,

$$Z = 1 - \frac{1}{F}\frac{\Delta T_4}{\Delta T_s},$$

The other parameters are defined as before. Ideally this procedure needs to be automated. There are several parameters that can be determined from the image data. These are:
(1) the clear-sky surface temperature T_s, (2) the cloud-top temperature T_c, (3) the clear-sky value of the water vapour correction, parametrised by b, and (4) the ratio of extinction coefficients β that governs the magnitude of the "U"-shaped distribution of negative differences.

A procedure for estimating these parameters from the image data has been developed. A brief outline is given below.

1. T_s. This is easily estimated by finding the maximum value of T_4 occurring in the data. A component for water vapour absorption correction is added using the method described earlier.

2. T_c. This is more difficult to estimate from the data, because the lowest value may not necessarily correspond to the volcanic cloud. However, provided an area in close proximity to the suspect cloud can be delineated it may be reasonable to assume that the lowest value is the cloud-top temperature.

3. b. This is estimated by evaluating $T_4 - T_5$ for the pixel corresponding to the maximum value of T_4. Then (2) is solved for b. Values of 3 to 5 appear to be acceptable.

4. β. Theoretical estimates of β suggest a value of around 0.7. A method for estimating β, T_s and T_c simultaneously has been developed by using the distribution of T_4 *vs* $T_4 - T_5$. The distribution is first histogrammed (or binned) into intervals of 0.5 K in T_4. Then, the lowest values in each bin are found and a curve is generated giving the outline of the distribution. The curve is smoothed and fitted using a nonlinear least squares model. The model has three parameters, *viz.*: T_s, $T_s - T_c$ and β that can be estimated from the fit.

The curve-fitting procedure uses the model developed earlier with $F = 1$ and the partial derivatives of the model, which are analytic. Writing,

$$Y = \alpha(X - X^\beta),$$

where, Y=T_4-T_5, α=T_s-T_c, X=1-$\frac{\gamma}{\alpha}$, γ=T_s-T_4. The partial derivatives are,

$$\frac{\partial Y}{\partial \alpha} = (X - X^\beta) + \frac{\gamma}{\alpha} + \beta\frac{\gamma}{\alpha}(1 - \frac{\gamma}{\alpha})^{\beta-1},$$

$$\frac{\partial Y}{\partial \beta} = \alpha X^\beta Log\beta,$$

$$\frac{\partial Y}{\partial \gamma} = 1 - \beta X^{\beta-1}.$$

An example of the curve-fitting procedure is shown in Figure 16. The distribution shown is for a volcanic ash plume from the 1996 June eruption of Ruapehu, New Zealand. The solid green-coloured lines are isolines of constant ash fraction F, and the red dots show the extrema of the distribution estimated from the data at constant temperature intervals. The extrema are used as input to Eq. (21) to determine the parameters of the model for F=1.0. Once these parameters are determined, F can be inferred for all pixels in the distribution.

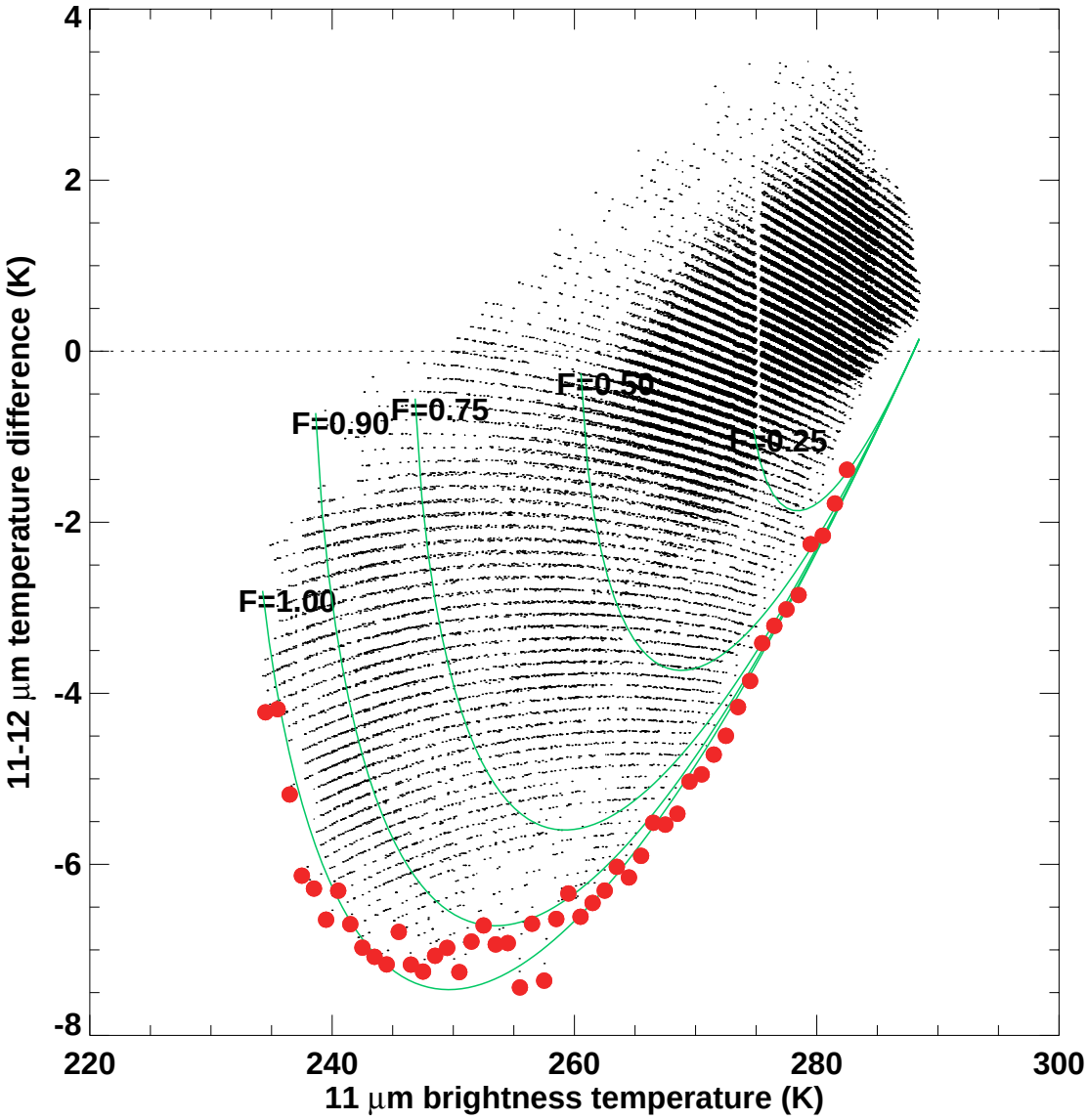

Figure 16. Distribution of $T_4 - T_5$ for an eruption of Ruapehu volcano. The green-coloured lines are isolines of the fraction of ash determined from Eq. (21). The red dots are estimates of the extrema of the distribution derived from the data.

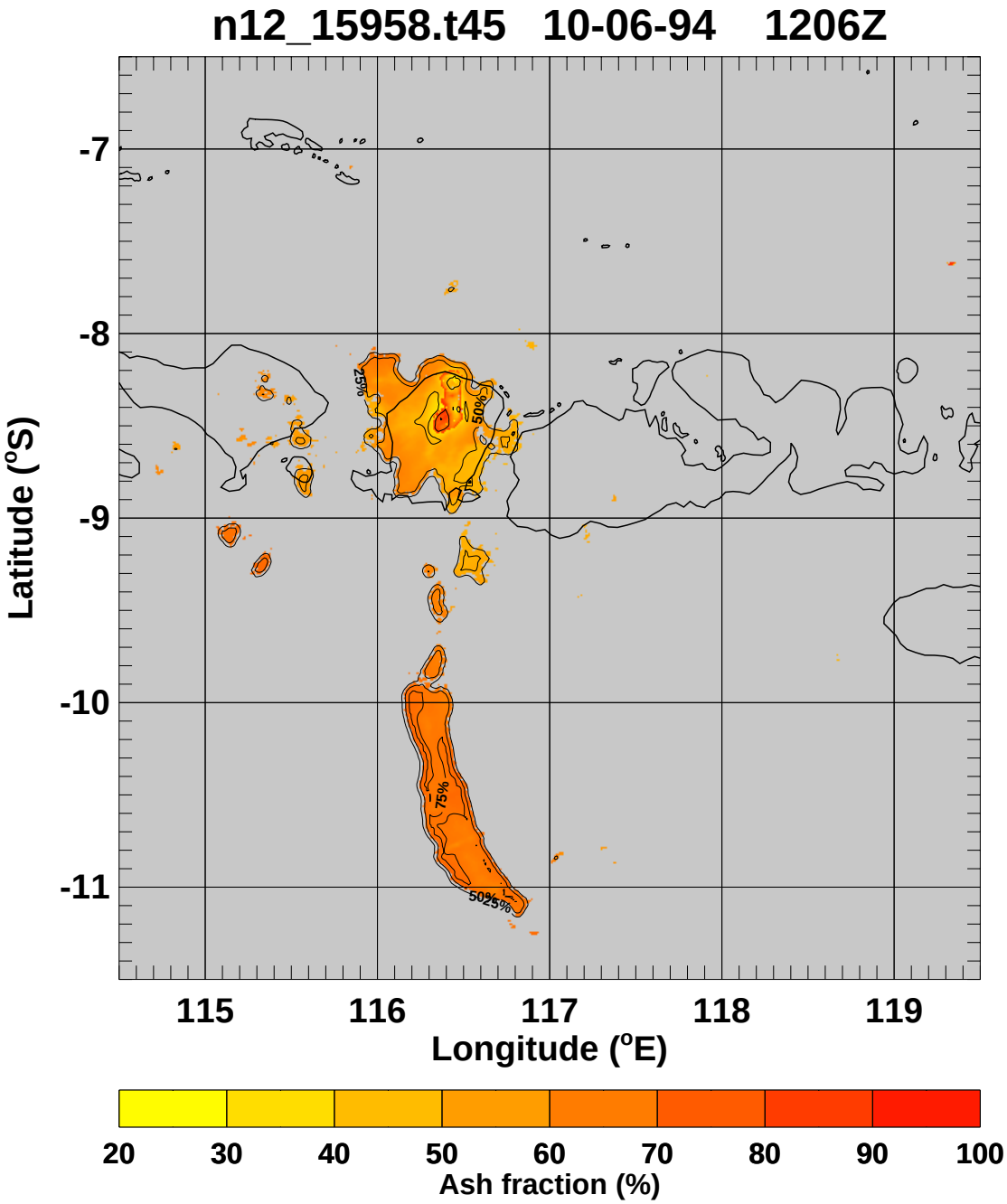

Figure 17. Ash fraction retrievals for eruption of Rindjani volcano, Indonesia. The colours and contours show the percentage of ash determined for each AVHRR pixel, assuming that the pixel contains a linear mixture of ash and water vapour components.

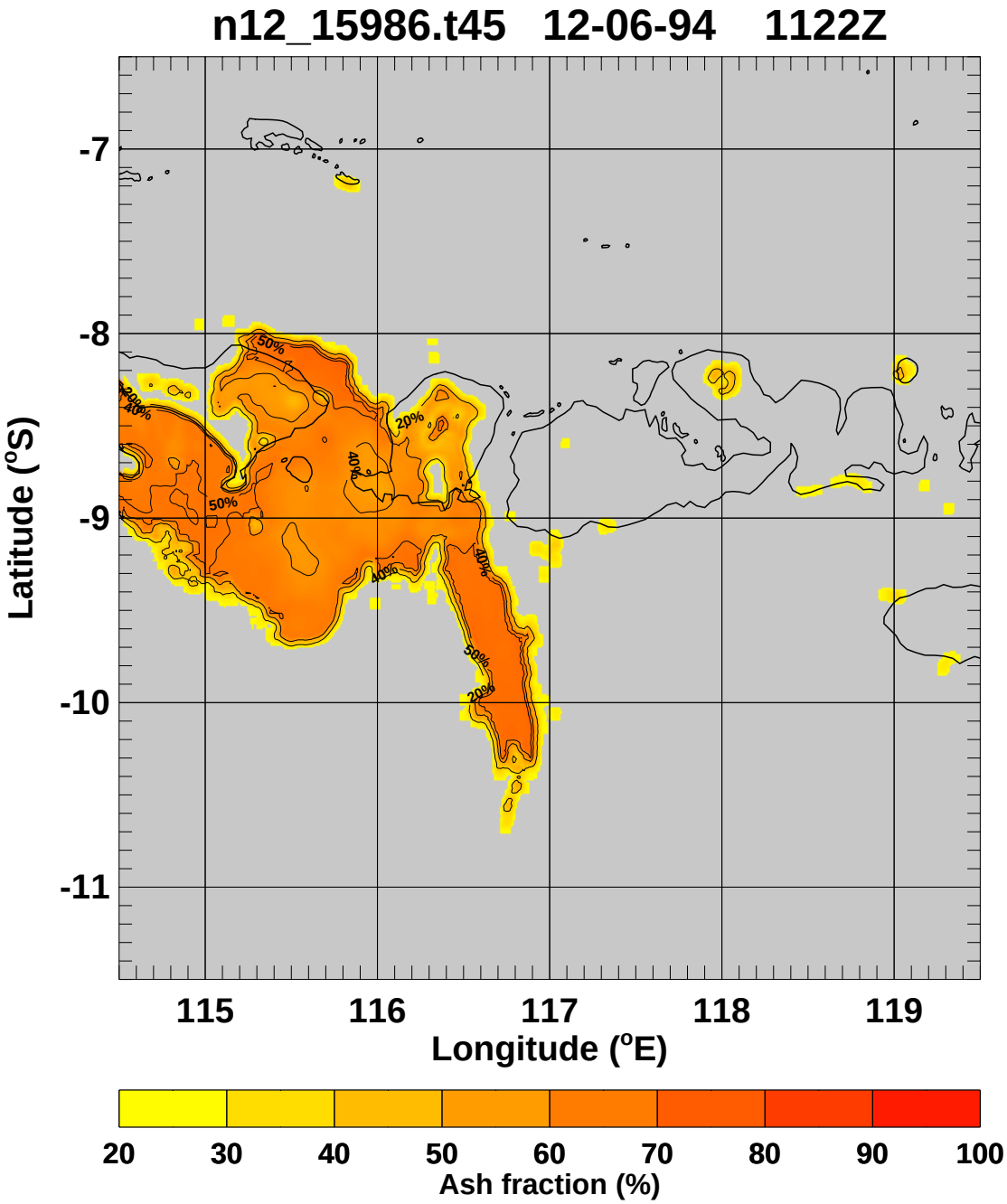

Figure 18. As for Fig. 17.

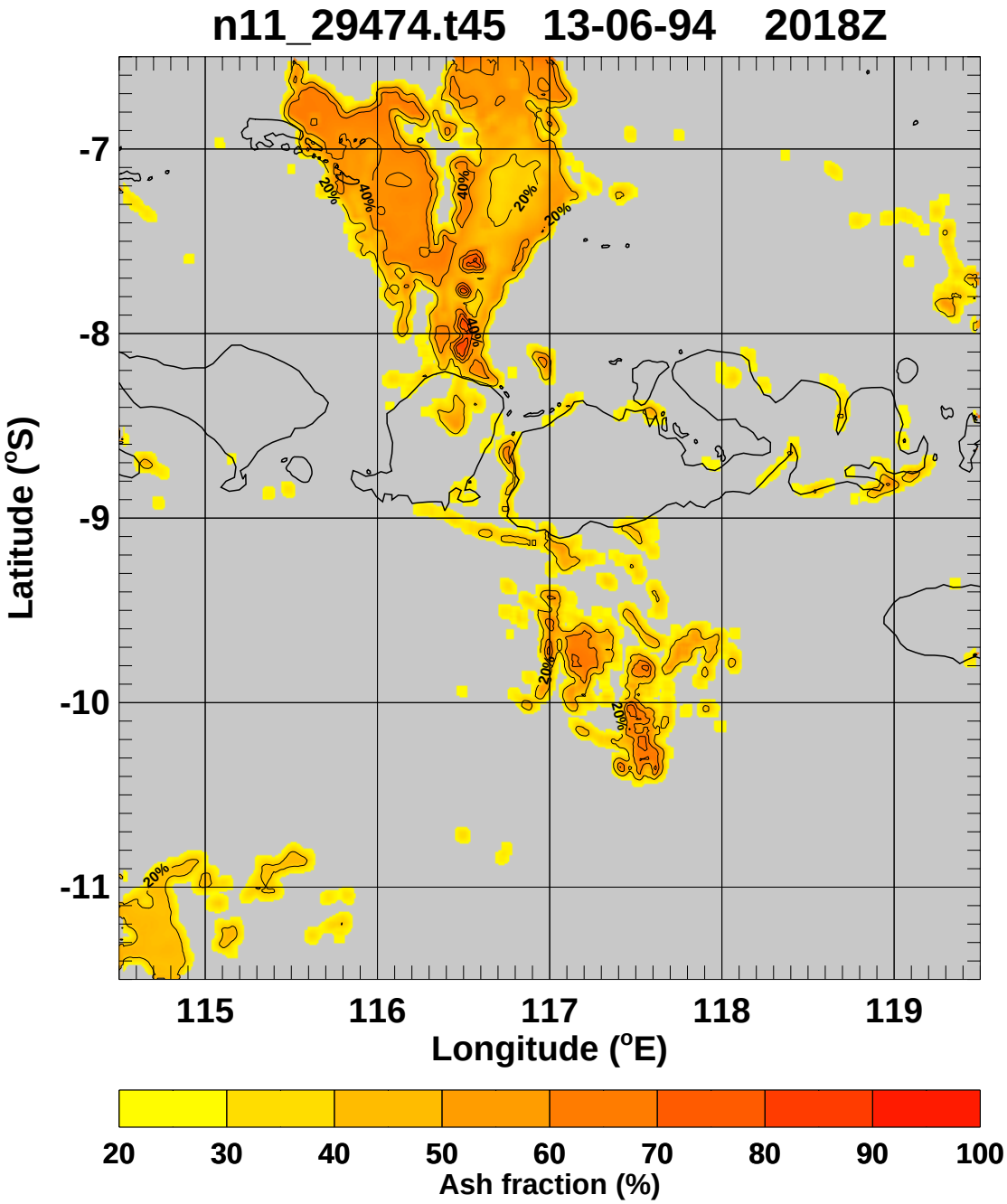

Figure 19. As for Fig. 17.

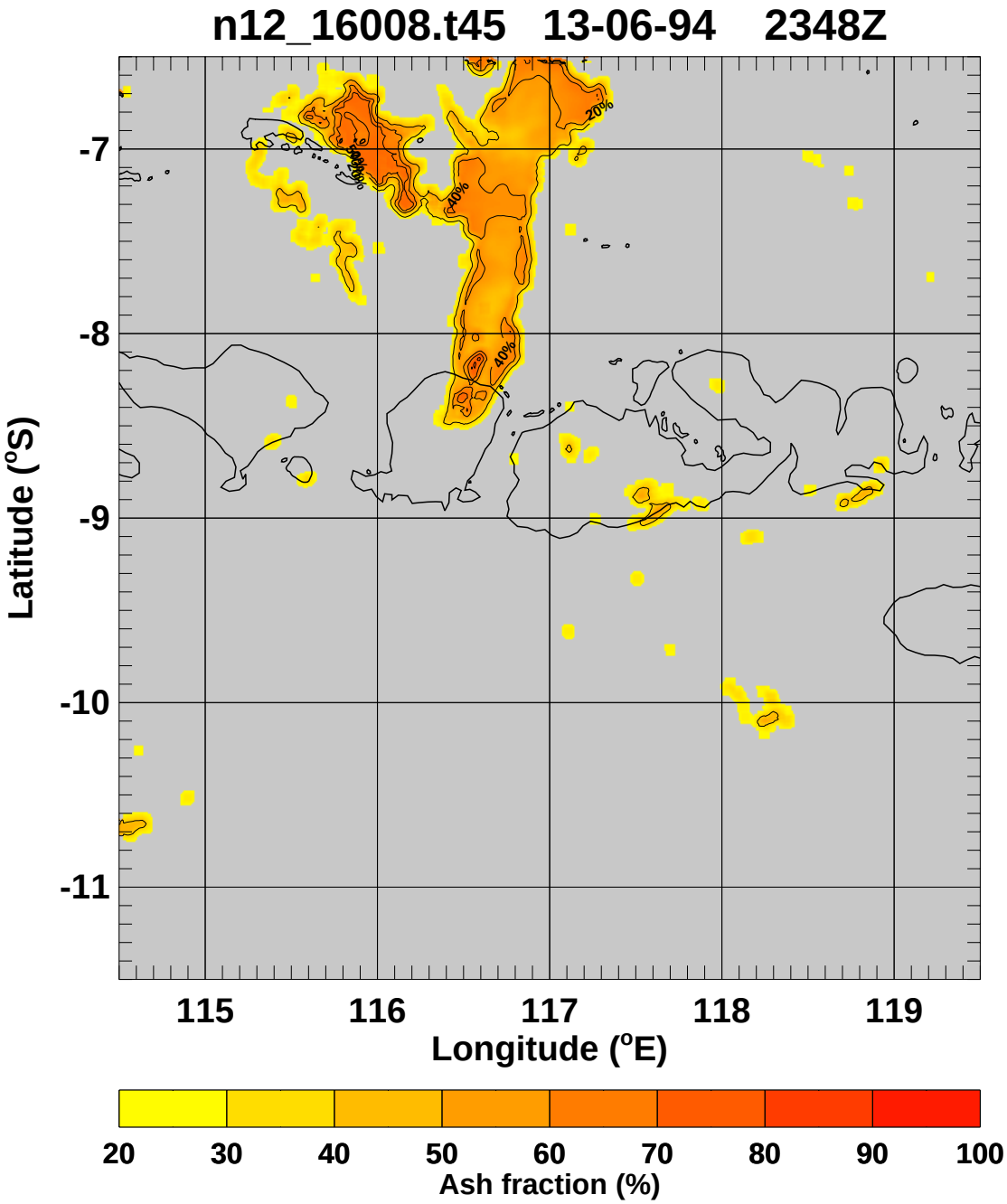

Figure 20. As for Fig. 17.

The ash fraction maps are an improvement over temperature difference images, but still suffer from ambiguities over land at night due to spectral emissivity effects for land surfaces. These can be overcome using a modified correction scheme that accounts for these spectral effects over the land. The correction simply allows for a lower emissivity at 11 μm than at 12 μm for pixels identified as land (using a map data-base) and have been applied to the nighttime images. Further improvements are likely by utilising a land cover scheme that identifies land pixels by their vegetation cover.

Another approach to water vapour correction is described by Yu *et al.* (2001). It is likely that many improvements in ash detection algorithms will be made in the coming years, especially with the advent of the new generation multispectral imagers.

8 Conclusions

A retrieval scheme for deriving the mean particle radius of fine particles, the optical depth and cloud-top height and mass loadings of volcanic clouds using infrared satellite data has been described. The scheme was tested using data from eruptions of the Ruapehu volcano in New Zealand. The optical parameters required to perform the retrievals are provided in tabular form in this report for wavelengths ranging from the visible to the thermal infrared.

Currently, there are just a few satellite-borne sensors that can take advantage of these parameters, but the advanced sensors, AATSR/MERIS, MODIS, GLI and SEVIRI will have multiple wavebands in the visible, near-infrared and thermal that may be used to exploit this new information. Table 4 lists the wavebands of these sensors and highlights which channels may be of the greatest use for volcanic ash retrievals.

The report also provides a scheme for correcting infrared data for the effects of water vapour and the methodology is illustrated using satellite data for some eruptions of Rindjani volcano in Indonesia.

Finally, in conjunction with the results reported in Prata and Grant (2001), this report should provide forecasters at Volcanic Ash Advisory Centres (VAACs) concerned with hazards to aviation new means for improving their warnings.

Table 4: Central wavelengths and bandpasses of the advanced sensors GLI, AATSR/MERIS, MODIS and SEVIRI. Channels likely to be useful for volcanic ash detection are in bold.

Central wavelength (μm)		*Bandpass (μm)*		Constituent
GLI	AATSR/MERIS	MODIS	SEVIRI	detected
Visible				
0.375		–	–	–
0.400		–	–	–
0.412	0.412	0.405–0.420	–	–
0.443	0.442	0.438–0.448	–	–
0.460		–	–	–
0.490	0.490	0.483–0.493	–	–
0.520	0.510	0.526–0.536	–	–
0.545		0.546–0.556	–	–
0.565	0.560	–	0.56–0.71	–
0.625	0.620	–	0.56–0.71	–
0.667	0.665	0.662-0.672	0.56–0.71	–
0.678	**0.681**	**0.673–0.683**	**0.56–0.71**	**Ash**
0.710	0.705	–	–	–
0.748	0.754	0.743–0.753	0.74–0.88	–
0.763	0.760	–	0.74–0.88	–
	0.775	–	0.74–0.88	–
0.865	0.865	0.862–0.877	0.74–0.88	–
	0.890	0.890–0.920	–	–
	0.900	0.915–0.965	–	–
Near infrared				
1.05		–	–	–
1.10		–	–	–
1.24		1.230–1.250	–	–
1.37		1.360–1.390	–	–
1.64	**1.61**	**1.628–1.652**	**1.50–1.78**	**Ash**
2.21		2.105–2.155		–
Thermal infrared				
3.72	**3.73**	**3.660–3.840**	**3.48–4.36**	**SO_2, Ash**
6.70			5.35–7.15	–
7.00			**6.85–7.85**	**SO_2**
7.30			**6.85–7.85**	**SO_2**
8.30			**8.30–9.10**	**SO_2, H_2SO_4, Ash**
–	–	–	9.38–9.94	
10.8	**10.8**		**9.80–11.80**	**H_2SO_4, Ash**
12.0	**12.0**		**11.00–13.00**	**H_2SO_4, Ash**
–	–	–	**12.40–14.40**	**Ash**

References

Berk, A., Bernstein, L. S., and Robertson, D. C.	1989	MODTRAN: A moderate resolution model for LOWTRAN 7, U. S., Air Force Phillips Laboratory, Nascom Air Force Base, MA, U. S. A., **AFGL-TR-89-0122.**
Briggs, G. A.	1975	Plume rise predictions. In *Lectures on Air Pollution and Environmental Impact Analyses*, pp. 59–111., American Meteorological Society, Boston.
Bursik, M. I., Sparks, R. S. J., Carey, S. N., and Gilbert, J. S.	1994	The concentration of ash in volcanic plumes, inferred from dispersal data, *In* Volcanic ash and aviation safety, *Proc. of the First International Symposium on Volcanic Ash and Aviation Safety*, US. Geological Survey Bulletin **2047**, Seattle, Washington, July, 1991. 19–29.
Cadle, R. D., Lazrus, A. L., Huebert, B. J., Heidt, L. E., Rose, W. I. Jr., Woods, D. C., Chuan, R. L., Stoiber, R. E., Smith, D. B., and Zielinski, R. A.	1979	Atmospheric implications of studies of Central American volcanic eruption clouds, *J. Geophys. Res.*, **84**(C11), 6961–6968.
Casadevall, T. J., (*Ed.*)	1994	Volcanic ash and aviation safety, *Proc. of the First International Symposium on Volcanic Ash and Aviation Safety*, US. Geological Survey Bulletin **2047**, Seattle, Washington, July, 1991.
Chuan, R. L., Woods, D. C. and McCormick, M. P.	1981	Characterisation of aerosols from eruptions of Mount St.Helens, *Science*,**211**, 830–832.
Davies, M. A., and Rose, W. I.,	1998	Evaluating GOES imagery for volcanic cloud observations at the Soufrière Hills volcano, Montserrat, *EOS Trans.*, AGU, **79**, 505–507.

Evans, B. T. N.	1988	An interactive program for estimating extinction and scattering properties of most particulate clouds, *Department of Defence Report* **MRL-R-1123**, Defence Science and Technology Organisation, Materials Research Laboratory, P.O. Box 50, Ascot Vale, Victoria 3032, Australia.
Hobbs, P. V., Radke, L. F., Eltgroth, M. W., and Hegg, D. A.	1981	Airborne studies of the emissions from the volcanic eruptions of Mount St.Helens, *Science*, **211**, 816–818.
Hofmann, D. J., and Rosen, J. M.	1984	Balloonborne particle counter observations of the El Chichón aerosol layers in the 0.01–1.8 μm radius range, *Geofisica International*, **23**, 155–185.
Ivlev, L. S., and Popova, S. I.	1973	The complex refractive indices of substances in the atmospheric-aerosol dispersed phase, *Atmospheric Oceanic Physics*, **9**(10), 587–591.
King, M. D., Harshvardhan, and Arking, A.	1984	A model of the radiative properties of the El Chichón stratospheric layer, *J. Climate Appl. Meteorol.*, **23**, 1121–1137.
Manins, P. C.	1985	Cloud heights and stratospheric injections resulting from a thermonuclear war, *Atmos. Environ.*, **19**(8), 1245–1255.
Masuda, K., and Takashima, T.	1990	Deriving cirrus information using the visible and near-ir channels of the future NOAA-AVHRR radiometer, *Remote Sens. Environ.*, **31**, 65—81.
Mossop, S. C.	1964	Volcanic dust collected at an altitude of 20 km, *Nature*, **203**, No. 4947, 824–827.
Mutlow, C. T.	1999	ATSR-1/2 User Guide, *Rutherford Appleton Laboratories Report*, 15 June, 1999 Issue 1, 29 pp. Also see `http://www.atsr.rl.ac.uk/user_documentation.html`.

Newell, R. E., and Deepak, A. (*Eds.*)	1982	Mount St. Helens eruptions of 1980: Atmospheric effects and potential climate impact, *NASA Workshop Report*, **NASA SP-458**, Scientific and Technical Information Branch, NASA, Washington, D. C., 119 pp.
Platt, C. M. R., and Stephens, G. L.	1980	The interpretation of remotely sensed high cloud emittances, *J. Atmos. Sci.*, **37**, 2314–2322.
Pollack, J. B., Toon, O. B., and Khare, B. N.	1973	Optical properties of some terrestrial rocks and glasses, *Icarus*, **19**, 372-389.
Prata, A. J.	1989a	Observations of volcanic ash clouds using AVHRR-2 radiances. *Int. J. Remote Sensing*, **10**(4-5), 751-761.
Prata., A. J.	1989b	Radiative transfer calculations for volcanic ash clouds, *Geophys. Res. Lett.*, **16**, 1293-1296.
Prata, A. J., and Grant, I. F.	2001	Retrieval of microphysical and morphological properties of volcanic ash plumes from satellite data: Application to Mt. Ruapehu, New Zealand, *Quart. J. Roy. Meteorol. Soc., In press.*
Prata, A. J. and Barton, I. J.	1994	Detection and discrimination of volcanic ash clouds by infrared radiometry – I: theory. In: Casadevall, T. J., editor. Volcanic Ash and aviation safety: proceedings of the first International Symposium on Volcanic Ash and Aviation Safety; Seattle, Wash. Washington, D.C.: U.S. G.P.O., *U.S. Geological Survey bulletin*, **2047**, 305-311.
Prata, A. J., and Turner, P. J.	1997	Cloud top height determination from the ATSR, *Rem. Sensing Environ.*, **59**, 1−13.
Press, W. H., Flannery, B. P., Teukolsky, S. A., and Vetterling, W. T.	1986	Numerical Recipes, *Cambridge University Press*, 818 pp.

Przedpelski, Z. J., and Casadevall, T. J.,	1994	Impact of volcanic ash from 15 December 1989 Redoubt volcano eruption on GE CF6-80C2 turbofan engines, *In Volcanic ash and aviation safety: Proc. of the First International Symposium on Volcanic Ash and Aviation Safety*, US. Geological Survey Bulletin **2047**, 129–135, Seattle, Washington, July, 1991.
Sokolik, I. N., and Toon, O. B.	1999	Incorporation of mineralogical composition into models of the radiative properties of mineral aerosol from UV to IR wavelengths, *J. Geophys. Res.*, **104** (D8), 9423–9444.
Stamnes, K. and Swanson, R. A.	1981	A new look at the discrete ordinates method for radiative transfer calculations in anisotropically scattering atmospheres, *J. Atmos. Sci.*, **38**, 387–399.
Volz, F. E.	1973	Infrared optical constants of ammonium sulfate, Sahara dust, volcanic pumice, and flyash, *Appl. Opt.*, **12**(3), 564-568.
Wen, S., and Rose, W. I.	1994	Retrieval of sizes and total masses of particles in volcanic clouds using AVHRR bands 4 and 5, *J. Geophys. Res.*, **99**(D3), 5421-5431.
Yu, T-X, and Rose, W. I.	1999	Retrieval of sulfate and silicate ash masses in young (1 to 4 days old) eruption clouds using multiband infrared HIRS/2 data, In *AGU Monograph on Remote Sensing of Active Volcanism*, **116**, American Geophysical Union, Washington, DC, 87–100.
Yu, T-X, Rose, W. I., and Prata, A. J.	2001	Atmospheric correction for satellite-based volcanic ash mapping and retrievals using 'split window' infrared data from GOES and AVHRR, *Submitted*.

Appendix. List of acronyms

AATSR–*Advanced Along-Track Scanning Radiometer*
ATSR–*Along-Track Scanning Radiometer*
AVHRR–*Advanced Very High Resolution Radiometer*
CRI–*Crown Research Institute*
CSIRO–*Commonwealth Scientific and Industrial Research Organisation*
DEM– *Digital Elevation Model*
ENVISAT–*Environmental Satellite*
ERS–*European Remote-sensing Satellite*
GIFTS–*Geostationary Imaging Fourier Transform Spectrometer*
GLI–*Global Imager*
GMS–*Geostationary Meteorological satellite*
GOES–*Geostationary Operational Environmental Satellite*
GVN–*Global Volcanism Network*
MERIS–*Medium Resolution Imaging Spectrometer*
MIPAS–*Michelson Interferometer for Passive Atmospheric Sounding*
MODIS–*Moderate resolution Imaging Spectroradiometer*
MTSAT–*Meteorological Satellite*
NOAA–*National Oceanographic and Atmospheric Administration*
SEVIRI–*Spinning Enhanced Visible Infrared Imager*
VAAC–*Volcanic Ash Advisory Centre*

CSIRO Atmospheric Research Technical Papers

This series has been issued as *Division of Atmospheric Research Technical Paper* (nos. 1–19); *CSIRO Division of Atmospheric Research Technical Paper* (nos. 20–37) and *CSIRO Atmospheric Research Technical Paper* from no. 38.

Regular electronic publication commenced with no. 45. Earlier technical papers are progressively being made available in electronic form. A current list of technical papers is maintained at *http://www.dar.csiro.au/info/TP.htm.*

Papers may be issued out of sequence.

No. 1 Galbally, I.E.; Roy, C.R.; O'Brien, R.S.; Ridley, B.A.; Hastie, D.R.; Evans, W.J.F.; McElroy, C.T.; Kerr, J.B.; Hyson, P.; Knight, W.; Laby, J.E. *Measurements of trace composition of the Austral stratosphere: chemical and meteorological data.* 1983. 31 p.

No. 2 Enting, I.G. *Error analysis for parameter estimates from constrained inversion.* 1983. 18 p.

No. 3 Enting, I.G.; Pearman, G.I. *Refinements to a one-dimensional carbon cycle model.* 1983. 35 p.

No. 4 Francey, R.J.; Barbetti, M.; Bird, T.; Beardsmore, D.; Coupland, W.; Dolezal, J.E.; Farquhar, G.D.; Flynn, R.G.; Fraser, P.J.; Gifford, R.M.; Goodman, H.S.; Kunda, B.; McPhail, S.; Nanson, G.; Pearman, G.I.; Richards, N.G.; Sharkey, T.D.; Temple, R.B.; Weir, B. *Isotopes in tree rings.* 1984. 86 p.

No. 5 Enting, I.G. *Techniques for determining surface sources from surface observations of atmospheric constituents.* 1984. 30 p.

No. 6 Beardsmore, D.J.; Pearman, G.I.; O'Brien, R.C. *The CSIRO (Australia) Atmospheric Carbon Dioxide Monitoring Program: surface data.* 1984. 115 p.

No. 7 Scott, John C. *High speed magnetic tape interface for a microcomputer.* 1984. 17 p.

No. 8 Galbally, I.E.; Roy, C.R.; Elsworth, C.M.; Rabich, H.A.H. *The measurement of nitrogen oxide (NO, NO_2) exchange over plant/soil surfaces.* 1985. 23 p.

No. 9 Enting, I.G. *A strategy for calibrating atmospheric transport models.* 1985. 25 p.

No. 10 O'Brien, D.M. *TOVPIX: software for extraction and calibration of TOVS data from the high resolution picture transmission from TIROS-N satellites.* 1985. 41 p.

No. 11 Enting, I.G.; Mansbridge, J.V. *Description of a two-dimensional atmospheric transport model.* 1986. 22 p.

No. 12 Everett, J.R.; O'Brien, D.M.; Davis, T.J. *A report on experiments to measure average fibre diameters by optical fourier analysis.* 1986. 22 p.

No. 13 Enting, I.G. *A signal processing approach to analysing background atmospheric constituent data.* 1986. 21 p.

No. 14 Enting, I.G.; Mansbridge, J.V. *Preliminary studies with a two-dimensional model using transport fields derived from a GCM.* 1987. 47 p.

No. 15 O'Brien, D.M.; Mitchell, R.M. *Technical assessment of the joint CSIRO/Bureau of Meteorology proposal for a geostationary imager/sounder over the Australian region.* 1987. 53 p.

No. 16 Galbally, I.E.; Manins, P.C.; Ripari, L.; Bateup, R. *A numerical model of the late (ascending) stage of a nuclear fireball.* 1987. 89 p.

No. 17 Durre, A.M.; Beer, T. *Wind information prediction study: Annaburroo meteorological data analysis.* 1989. 30 p. + diskette.

No. 18 Mansbridge, J.V.; Enting, I.G. *Sensitivity studies in a two-dimensional atmospheric transport model.* 1989. 33 p.

No. 19 O'Brien, D.M.; Mitchell, R.M. *Zones of feasibility for retrieval of surface pressure from observations of absorption in the A band of oxygen.* 1989. 12 p.

No. 20 Evans, J.L. *Envisaged impacts of enhanced greenhouse warming on tropical cyclones in the Australian region.* 1990. 31 p. [Out of print]

No. 21 Whetton, P.H.; Pittock, A.B. *Australian region intercomparison of the results of some general circulation models used in enhanced greenhouse experiments.* 1991. 73 p. [Out of print]

No. 22 Enting, I.G. *Calculating future atmospheric CO_2 concentrations.* 1991. 32 p.

No. 23 Kowalczyk, E.A.; Garratt, J.R.; Krummel, P.B. *A soil-canopy scheme for use in a numerical model of the*

atmosphere — 1D stand-alone model. 1992. 56 p.

No. 24 Physick, W.L.; Noonan, J.A.; McGregor, J.L.; Hurley, P.J.; Abbs, D.J.; Manins, P.C. *LADM: A Lagrangian Atmospheric Dispersion Model.* 1994. 137 p.

No. 25 Enting, I.G. *Constraining the atmospheric carbon budget: a preliminary assessment.* 1992. 28 p.

No. 26 McGregor, J.L.; Gordon, H.B.; Watterson, I.G.; Dix, M.R.; Rotstayn, L.D. *The CSIRO 9-level atmospheric general circulation model.* 1993. 89 p.

No. 27 Enting, I.G.; Lassey, K.R. *Projections of future CO_2.* with appendix by R.A. Houghton. 1993. 42 p.

No. 28 [Not published]

No. 29 Enting, I.G.; Trudinger, C.M.; Francey, R.J.; Granek, H. *Synthesis inversion of atmospheric CO_2 using the GISS tracer transport model.* 1993. 44 p.

No. 30 O'Brien, D.M. *Radiation fluxes and cloud amounts predicted by the CSIRO nine level GCM and observed by ERBE and ISCCP.* 1993. 37 p.

No. 31 Enting, I.G.; Wigley, T.M.L.; Heimann, M. *Future emissions and concentrations of carbon dioxide: key ocean/atmosphere/land analyses.* 1993. 120 p.

No. 32 Kowalczyk, E.A.; Garratt, J.R.; Krummel, P.B. *Implementation of a soil-canopy scheme into the CSIRO GCM – regional aspects of the model response.* 1994. 59 p.

No. 33 Prata, A.J. *Validation data for land surface temperature determination from satellites.* 1994. 36 p.

No. 34 Dilley, A.C.; Elsum, C.C. *Improved AVHRR data navigation using automated land feature recognition to correct a satellite orbital model.* 1994. 22 p.

No. 35 Hill, R.H.; Long, A.B. *The CSIRO dual-frequency microwave radiometer.* 1995. 16 p.

No. 36 Rayner, P.J.; Law, R.M. *A comparison of modelled responses to prescribed CO_2 sources.* 1995. 84 p.

No. 37 Hennessy, K.J. *CSIRO Climate change output.* 1998. 23 p.

No. 38 Enting, I.G. *Attribution of greenhouse gas emissions, concentrations and radiative forcing.* 1998. 27 p.

No. 39 O'Brien, D.M.; Tregoning, P. *Geographical distributions of occultations of GPS satellites viewed from a low earth orbiting satellite.* (1998) 28p.

No. 40 Enting, I.G. *Characterising the temporal variability of the global carbon cycle.* 1999. 53 p.
Also electronic edition at *http://www.dar.csiro.au/publications/Enting_2000a.pdf.*

No. 41 (in preparation).

No. 42 Mitchell, R.M. *Calibration status of the NOAA AVHRR solar reflectance channels: CalWatch revision 1.* 1999. 20 p.

No. 43 Hurley, P.J. *The Air Pollution Model (TAPM) Version 1: technical description and examples.* 1999. 41 p.
Also electronic edition at *http://www.dar.csiro.au/publications/Hurley_1999a.pdf*

No. 44 Frederiksen, J.S.; Dix, M.R.; Davies, A.G. *A new eddy diffusion parameterisation for the CSIRO GCM.* 2000. 31 p.

No. 45 Young, S.A. *Vegetation Lidar Studies.*
Electronic edition only. At *http://www.dar.csiro.au/publications/Young_2000a.pdf.*

No. 46 Prata, A. J. *Global Distribution of Maximum Land Surface Temperature Inferred from Satellites: Implications for the Operation of the Advanced Along Track Scanning Radiometer.* 2000. 30 p.
Electronic edition only. At *http://www.dar.csiro.au/publications/Prata_2000a.pdf.*

No. 47 Prata, A. J. *Precipitable water retrieval from multi-filter rotating shadowband radiometer measurements.* 2000. 14 p. Electronic edition only. At *http://www.dar.csiro.au/publications/Prata_2000b.pdf.*

Address and contact details: CSIRO Atmospheric Research
Private Bag No.1 Aspendale Victoria 3195 Australia
Ph: (+61 3) 9239 4400; fax: (+61 3) 9239 4444
e-mail: chief@dar.csiro.au